



Thermal catalysis vs. photocatalysis: A case study with $\text{FeVO}_4/\text{g-C}_3\text{N}_4$ nanocomposites for the efficient activation of aromatic and benzylic C–H bonds to oxygenated products

Subhajyoti Samanta, Rajendra Srivastava *

Department of Chemistry, Indian Institute of Technology Ropar, Rupnagar, Punjab, 140001, India



ARTICLE INFO

Article history:

Received 24 March 2017

Received in revised form 28 May 2017

Accepted 16 June 2017

Available online 17 June 2017

Keywords:

FeVO_4

$\text{g-C}_3\text{N}_4$

Oxidation

Hydroxylation

Visible light photocatalysis

ABSTRACT

Three semiconductor metal vanadates FeVO_4 , BiVO_4 , and LaVO_4 were synthesized. To improve the thermal catalytic and photocatalytic activity of highly efficient metal vanadate FeVO_4 , nanocomposites of FeVO_4 and graphitic C_3N_4 were prepared. Nanocomposites were prepared via thermal annealing method by varying the composition of FeVO_4 and $\text{g-C}_3\text{N}_4$. Catalysts were characterized by a series of complementary combination of powder X-ray diffraction, thermogravimetric analysis, N_2 adsorption-desorption, scanning/transmission electron microscopy, energy dispersive X-ray analysis, Fourier transform infrared spectroscopy, diffuse reflectance ultraviolet-visible spectroscopy, X-ray photoelectron spectroscopy, photoluminescence, and photoelectrochemical techniques. Catalysts were investigated in the liquid phase oxidation of benzene, phenol, hydroquinone, naphthalene, anthracene, toluene, ethyl benzene, di-phenyl methane, and *p*-xylene under conventional thermal condition and visible light irradiation condition. Kinetic and thermodynamic parameters (such as k , E_a , ΔH , ΔG , and ΔS) were calculated for the benzene hydroxylation by varying the reaction parameters under thermal catalytic condition. In order to confirm the active species responsible for the thermal catalytic and photocatalytic processes, UV-vis, fluorescence, cyclic voltammetry, and radical scavenging experiments were carried out with the help of suitable probe molecules. Based on the results obtained, reaction mechanism was proposed, and the structure-activity relationship was established. The catalyst was magnetically separated and recycled with negligible loss in the activity which is important for the sustainable heterogeneous catalysis. The developed catalytic process has the potential for the sustainable synthesis of a wide range of industrially important fine chemicals. Such a unique and detailed investigation of comparative study between thermal catalysis and photocatalysis using $\text{FeVO}_4/\text{g-C}_3\text{N}_4$ nanocomposite will be highly useful to design optimum catalyst for an appointed catalytic reaction.

© 2017 Elsevier B.V. All rights reserved.

1. Introduction

Activation of aromatic and benzylic C–H bonds to oxygenated products is an attractive route to synthesize a wide range of important fine chemicals such as phenol, benzoquinone, acetophenone, etc. Phenol is widely used in the synthesis of phenol resin, bisphenol-A, caprolactam, etc. Further, benzaldehyde and acetophenone are extensively utilized to produce a wide range of synthetic intermediates through C=O group transformation. Similarly, quinones are important precursors for the synthesis of many valuable chemicals that exhibit cardiovascular, antitumor,

antibacterial, antigerminative, and antiprotozoal activities [1–3]. In conventional practice, syntheses of these compounds are not straight forward. For example, phenol is industrially produced from surplus cumene as a petroleum feedstock by Hock process, in which cumene is oxidized to cumene hydroperoxide by air in aqueous Na_2CO_3 followed by the acid treatment to produce equivalents amount of phenol and acetone [4]. Benzaldehyde is produced by the side-chain chlorination of toluene followed by saponification of the resulting dichloromethyl group [5]. However, this process leads to produce benzaldehyde (which is contaminated with the chlorinated by-products) that do not meet FDA protocols. Moreover, benzaldehyde can also be produced by the vapour phase oxidation of toluene with oxygen [6,7]. The vapour phase process is operated at high pressure and temperature which is too harsh to improve the selectivity of the benzaldehyde. Acetophenone is produced by the oxidation of ethylbenzene in the homogeneous catalytic process

* Corresponding author.

E-mail address: rajendra@iitrpr.ac.in (R. Srivastava).

using cobalt acetate or cobalt cycloalkane carboxylate as catalyst, manganese and/or bromide species as promoters, acetic acid as a solvent and molecular oxygen or air as an oxidant [8]. Corrosive nature of acetic acid, difficulty in the solvent, and catalyst recovery, and explosion hazards associated with the solvent and dioxygen discourage this industrial process. Furthermore, benzoquinone can be prepared by the oxidation of hydroquinone [9,10].

One can easily think that these compounds can be prepared by the direct functionalization of aromatic hydrocarbons by the catalytic oxidation of C–H bonds to form oxygenated products under mild reaction condition using H_2O_2 as a safe oxidizing agent. Various metal oxide and zeolite based catalysts have been developed for these reactions [11–15]. Microporous titanosilicate is one of the most studied catalysts for the hydroxylation and epoxidation reactions involving small organic molecules [11,12]. Researchers have developed mesoporous titanosilicate and zirconosilicate for reactions involving large organic molecules [13–15]. Vanadium containing mesoporous silicate and polyoxometalates have also been developed for the aromatic C–H activation [16–18]. Further, Fe-based Fenton reagent is well known for the hydroxylation reaction. Therefore, efforts have been made to develop Fe-based heterogeneous catalysts for C–H activation [19–21]. However, low yield of the product was obtained using Fe/V/Ti based metallocilicates using TBHP or H_2O_2 . It is difficult to incorporate a large amount of metal in zeolite/silica framework, which is one of the prime reason for the low catalytic activity. Furthermore, the mild acidic nature of zeolite framework is responsible for the low selectivity of the desired product, especially in the epoxidation reaction. This problem can be solved if Fe/V/Ti-based catalyst is supported on a neutral support such as carbon or related materials. In this study, we demonstrated the application of C_3N_4 as support material, which is being explored as a versatile support for the heterogeneous catalysis [22,23]. It is worthy to note that C_3N_4 based materials are being developed due to their excellent photocatalytic activity [24–31]. Photochemical dissociation of H_2O_2 can produce various oxygenated free radicals. Such free radicals are known to catalyze oxidation reactions and the degradation of organic pollutants found in water bodies [32–35].

Mixed metal oxides containing two or more metals are widely used as commercial catalysts for various industrial processes. Since V and Fe have been found to be good metals for the catalytic oxidation, therefore one may anticipate that oxide of these metals could be interesting for C–H activation also. $FeVO_4$ has been studied for a few oxidation reactions such as methanol oxidation [36,37]. $FeVO_4$ also exhibited impressive results in the gas sensing [38,39]. The role of $FeVO_4$ as a heterogeneous catalyst is less explored. However, in the recent time, significant efforts are being made to develop $FeVO_4$ based photocatalysts [40,41].

In the present study, metal vanadates ($FeVO_4$, $BiVO_4$, and $LaVO_4$) were investigated in the liquid phase oxidation of aromatic compounds for the synthesis of phenol, hydroquinone, benzoquinone, 1,4-napthoquinone, 9,10-anthraquinone, benzaldehyde, acetophenone, 4-methyl benzaldehyde, and benzophenone using H_2O_2 under mild reaction condition. For further improvement in the catalytic activity, $FeVO_4$ and $g-C_3N_4$ based nanocomposites were prepared and investigated in the synthesis of above mentioned compounds. The detailed kinetic investigation was carried out by varying the reaction parameters such as substrate concentration, catalyst amount, H_2O_2 amount, and temperature. H_2O_2 efficiency and thermodynamic parameters such as activation energy (E_a), change of – enthalpy (ΔH), Gibbs free energy (ΔG), and entropy (ΔS) were calculated. Time-dependent UV–vis study was performed to investigate the active species involved in the oxidation reaction. Further, reactions were performed in the presence of radical scavenger to verify the intermediate radical species involved in the reaction.

$FeVO_4$ and $g-C_3N_4$ have good visible light absorption capacity and good photocatalytic activity. In this study, $FeVO_4/g-C_3N_4$ nanocomposite catalysts were investigated in the C–H activation at ambient temperature under visible light irradiation and the results were compared with the data obtained under thermal catalytic condition. The unique aspect of this study is to demonstrate the difference in the catalytic activity of $FeVO_4$ and $FeVO_4/g-C_3N_4$ nanocomposites under conventional thermal catalysis and photocatalysis. Catalysts exhibited better activity under photocatalytic condition when compared to thermal catalysis. Involvement of radical species in the photoassisted reaction was confirmed by fluorescence spectrometer with radical trapping experiments using terephthalic acid as a probe molecule. Involvement of hydroxyl radical species was also confirmed using cyclic voltammetry. Catalyst was easily separated using magnet and recycled with negligible loss in the activity during thermal catalysis and photocatalysis. Catalytic investigations reveal that $FeVO_4/g-C_3N_4$ (3:7) exhibited the highest catalytic activity among all the catalysts investigated in this study with good recovery and excellent recyclability. The excellent catalytic activity of $FeVO_4/g-C_3N_4$ (3:7) nanocomposite under thermal catalytic and photocatalytic conditions can be attributed to the dual metal catalysis by Fe^{+3} & V^{+5} , optimum dispersion of $FeVO_4$ nanospheres on $g-C_3N_4$ matrix, optimum physical adsorption and photo-physical processes like photoadsorption, photodesorption, and efficient charge separation. The key features of the present study is that the same material ($FeVO_4/g-C_3N_4$ nanocomposite) is able to catalyze same set of reactions under thermal condition as well as under visible light illumination which will encourage catalysis researchers, materials chemists, and green & sustainable chemists to develop novel catalysts for the synthesis of a wide range of fine chemicals.

2. Experimental

2.1. Materials

All chemicals were of AR grade and used as received without further purification. $Fe(NO_3)_3 \cdot 6H_2O$, NH_4VO_3 , melamine, and ethanol were obtained from Loba Chemie Pvt. Ltd. India. Benzene, phenol, hydroquinone, naphthalene, anthracene, toluene, ethyl benzene, *p*-xylene, and diphenyl methane were purchased from Spectrochem India Pvt. Ltd. Hydrogen peroxide and acetonitrile were obtained from Merck Chemicals, India.

2.2. Catalyst preparation

2.2.1. Synthesis of $FeVO_4$

$FeVO_4$ was prepared by following the reported procedure [42]. In a typical synthesis, 80 mL of 0.3 M NH_4VO_3 and 80 mL of 0.3 M $Fe(NO_3)_3 \cdot 6H_2O$ were mixed in a beaker and stirred until a yellow precipitation appeared. Reaction mixture was transferred into a Teflon-lined stainless steel autoclave and kept in an oven at 180 °C for 3 h. Autoclave was cooled to ambient temperature and the reaction mixture was centrifuged. Solid product was washed with deionized water followed by ethanol, and dried in vacuum at 60 °C for 6 h. Finally, the resulting sample was calcined at 550 °C for 24 h. Details of synthesis procedure for $BiVO_4$ and $LaVO_4$ are provided in supporting information section.

2.3. Synthesis of $g-C_3N_4$

Graphitic carbon nitride was synthesized by heating 10 g of melamine in a cylindrical crucible (closed with a lid) at 550 °C for 4 h at a heating rate of 5 °C/min in a programmable furnace [24].

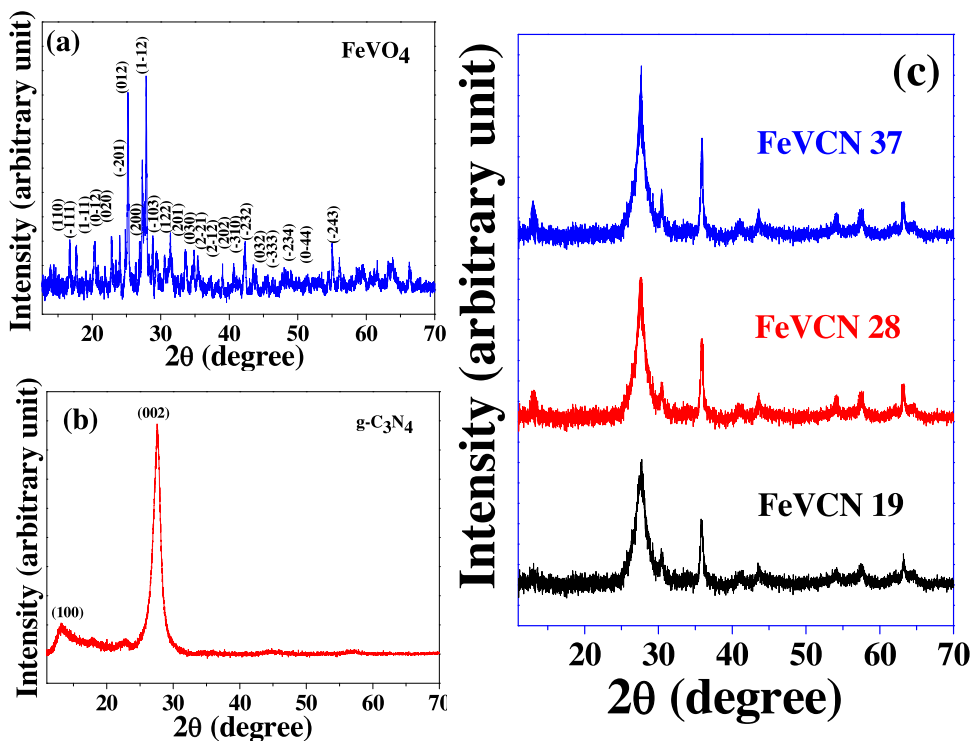


Fig. 1. XRD patterns of (a) FeVO₄, (b) g-C₃N₄ and (c) FeVO₄/g-C₃N₄ nanocomposites investigated in this study.

The furnace was allowed to cool to ambient temperature naturally. Solid g-C₃N₄ was collected and grinded (Yield = 5.2 g).

2.4. Synthesis of FeVO₄/g-C₃N₄ nanocomposite

The different weight percentage of FeVO₄ was loaded on g-C₃N₄ by a solid state combustion method. In a typical synthesis of FeVO₄/g-C₃N₄(2:8), 20 mg of FeVO₄ and 80 mg of g-C₃N₄ were homogeneously grinded with a mortar pestle in the presence of 2 mL of ethanol. The resulting material was dried at 200 °C for 2 h in an oven and then calcined at 400 °C for 4 h in a programmable furnace. The material is designated as FeVCN 28. Using the similar procedure, FeVCN 19, FeVCN 37, and FeVCN 55 were also prepared. Step-wise synthesis strategy followed in this study is presented in Scheme S1, ESI.

2.5. Catalyst characterization & catalytic reactions

Details of material characterization, procedure for the photoelectrochemical study, and procedures for the photocatalytic/thermal catalytic reactions are presented in supporting information section, ESI.

3. Results and discussion

3.1. Physico-chemical characterization

The crystal structure and phase purity of the synthesized materials were confirmed by powder X-ray diffraction analysis (XRD) (Fig. 1). FeVO₄ exhibits intense reflections similar to that of the triclinic crystal system (JCPDS file number 14-0688) which is in good agreement with reported literature (Fig. 1a) [42]. Graphitic carbon nitride (g-C₃N₄) exhibits two reflections at 12.6° and 27.4° which can be indexed to 100 and 220 graphitic planes, corresponding to the in-plane structural packing motif and interlayer stacking peak of aromatic systems, respectively (Fig. 1b) [43]. The d spacing for

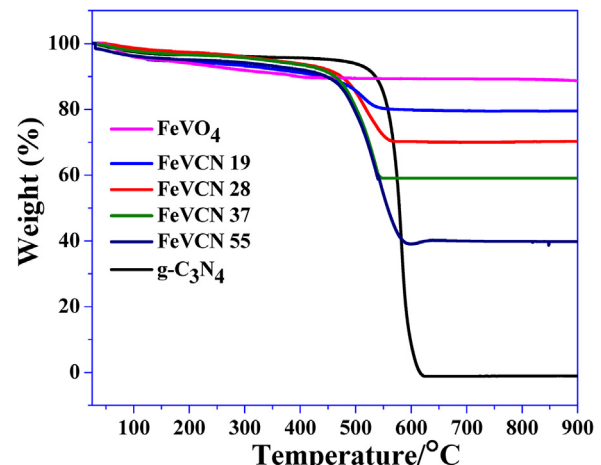


Fig. 2. Thermograms of various materials prepared in this study.

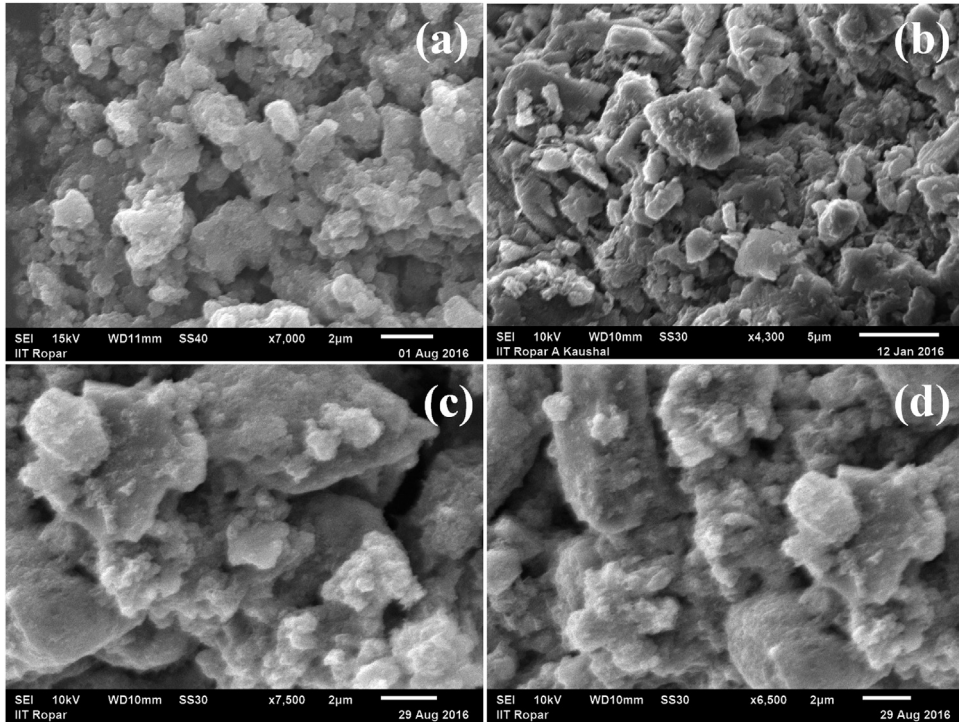
these two planes 100 and 220 are found to be 0.698 and 0.325 nm, respectively, which are identical with the reported g-C₃N₄ [46]. XRD patterns of FeVO₄/g-C₃N₄ composites exhibit reflections associated with both triclinic FeVO₄ and g-C₃N₄ (Fig. 1c). The XRD patterns of FeVO₄/g-C₃N₄ composites are dominant with the reflections associated with g-C₃N₄. The XRD patterns of LaVO₄ and BiVO₄ matched well with the reported literature (Fig. S1 (a) and (b)).

Thermal stability of the material was studied by thermogravimetric analysis (TGA) (Fig. 2). Thermogram of FeVO₄ shows that the material exhibits high thermal stability (even more than 900 °C). The small amount of weight loss in FeVO₄ is attributed to the removal of water molecules by the condensation of surface hydroxyl groups upon heating [44]. Thermogram of g-C₃N₄ shows that the decomposition starts at 490 °C and extends up to 620 °C. The signature of the thermograms for various nanocomposites prepared in this study is similar to that of the g-C₃N₄ and provides the evidence for the percentage composition of g-C₃N₄.

Table 1

Textural properties of various catalysts investigated in this study.

Catalyst	Surface area(m ² /g)	External surface area (m ² /g)	Mesopore volume (cc/g)	Total pore volume (cc/g)
FeVO ₄	27.2	23.1	0.040	0.046
g-C ₃ N ₄	20.8	20.2	0.047	0.048
FeVCN 19	35.4	34.2	0.052	0.053
FeVCN 28	45.3	44.8	0.067	0.069
FeVCN 37	54.6	54.2	0.081	0.083
FeVCN 55	42.8	41.7	0.064	0.067
FeVCN 37 (reused)	53.7	53.1	0.080	0.082

**Fig. 3.** SEM images of (a) FeVO₄, (b) g-C₃N₄, (c) FeVCN 19, and (d) FeVCN 37.

and FeVO₄. The percentage composition (wt%) of (FeVO₄:g-C₃N₄) obtained from TGA analysis for FeVCN 19, FeVCN 28, FeVCN 37, and FeVCN 55 were found to be (9.9:90.1), (19.3:80.7), (30.2:69.8), and (50.6: 49.4), respectively, which are close to the input composition.

The nitrogen adsorption–desorption isotherms for FeVO₄, g-C₃N₄, and FeVCN 37 are presented in Fig. S2, ESI. FeVO₄ exhibited a type II isotherm with no hysteresis loop, whereas g-C₃N₄ and FeVCN 37 exhibited type IV isotherm with a H3 hysteresis. g-C₃N₄ and FeVCN 37 exhibited a broad pore size distribution. The surface area and pore volume of nanocomposite FeVCN 37 were found to be more when compared to their individual constituents, FeVO₄ and g-C₃N₄. Textural properties of various materials prepared in this study are provided in **Table 1**.

Morphology and microstructure of different materials prepared in present study were investigated using scanning/transmission electron microscope (SEM/TEM). Aggregated nanocrystals like surface morphology was observed for FeVO₄ (Fig. 3a), whereas a flake-like morphology was observed for g-C₃N₄ (Fig. 3b). A mixed morphology can be seen in the SEM micrographs of nanocomposite materials (Figs. 3 c, d and S3, ESI). The elemental composition of different materials prepared in present study was evaluated from the energy dispersive X-ray analysis (EDX). The EDX spectra (Fig. S4, ESI) obtained from different materials (Fig. S4, ESI) clearly shows the presence of various constituent elements present in the sample and confirmed the formation of nanocomposites of g-C₃N₄ and

FeVO₄. BiVO₄ and LaVO₄ also exhibited irregular crystal morphologies (Fig. S5, ESI).

The detailed micro/nanostructure of FeVO₄ and FeVCN 37 was studied using high resolution transmission electron microscope (HRTEM) (Fig. 4). The bright field HRTEM image of FeVO₄ shows spherical shape nanoparticles with a size distribution between 15 and 20 nm (Fig. 4a and b). The TEM image of the best performing catalyst, FeVCN 37, clearly shows that FeVO₄ nanospheres are uniformly dispersed on the g-C₃N₄ matrix (Fig. 4c and d). HRTEM image contains dark gray and light gray areas that represent the FeVO₄ and g-C₃N₄ domains. The lattice resolved HRTEM captured for FeVCN 37 composite exhibits lattice fringes for both FeVO₄ and g-C₃N₄. The measured lattice spacing of 0.234 nm and 0.119 nm was obtained for FeVO₄ and g-C₃N₄ that matched well with the d spacing correspond to (111) plane of FeVO₄ and (022) plane of g-C₃N₄, respectively, (Fig. 4e) [45,46]. The selected area electron diffraction pattern captured by focusing electron beam on the sample indicates the presence of concentric ring containing diffractions from both, FeVO₄ and g-C₃N₄, in the resulting nanocomposite FeVCN 37 (Fig. 4f). Further, the ring pattern indicates polycrystalline nature of the composite.

Light absorption and opto-electronic properties of various materials prepared in this study were characterized by the diffuse reflectance UV–vis spectroscopy (DRUV-vis) (Fig. 5a). g-C₃N₄ exhibited an absorbance edge around 475 nm whereas FeVO₄ exhibited an absorbance edge around 630 nm [44,46]. UV–vis spec-

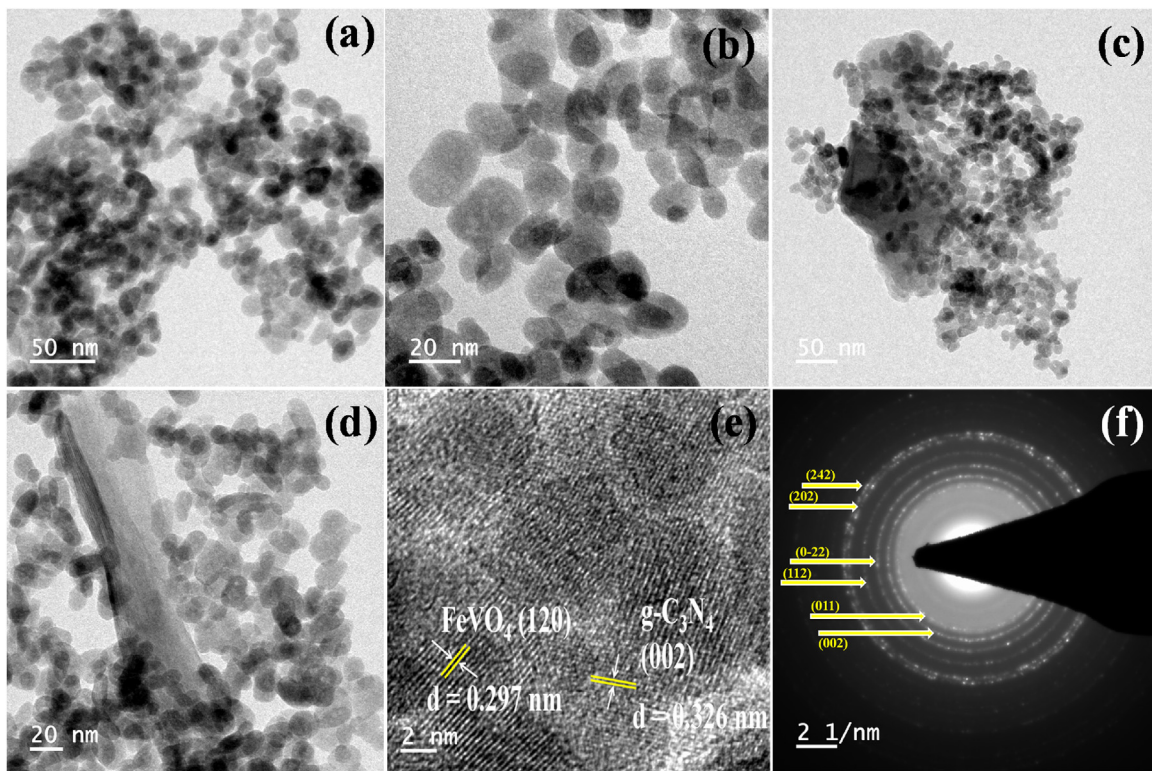


Fig. 4. TEM images of (a, b) FeVO₄, (c–e) FeVCN 37, and (f) SAED pattern obtained from image (e).

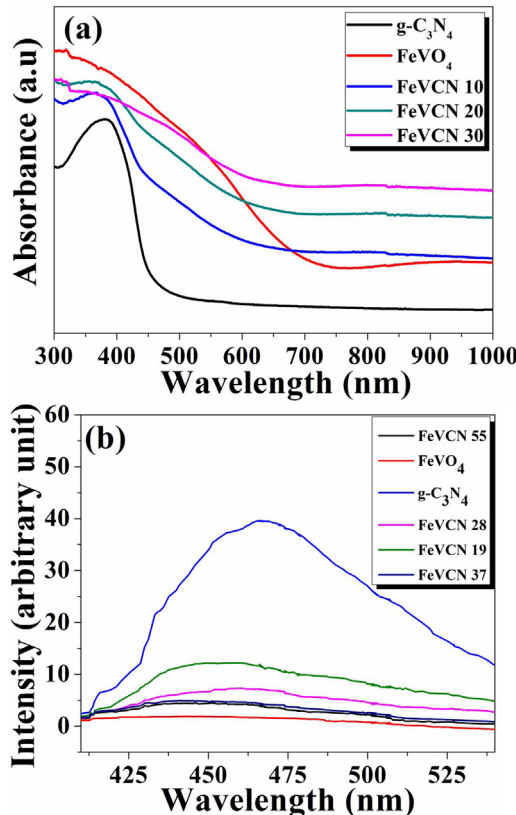


Fig. 5. (a) DRUV-vis spectra and (b) Photoluminescence spectra of various materials investigated in this study.

tra show that the absorption edge lies in the range of 475–575 nm for various nanocomposites prepared in this study. The band gap

energy for all the materials was calculated using $\alpha h\nu = k(h\nu - E_g)^{n/2}$ where, E_g represents the band gap of the corresponding semiconductor, $h\nu$ is the photon energy, k is the constant, α is the Kubelka–Munk function, and n is dependent on the type of transition involved [45]. For a semiconductor photocatalyst the fate of the transition, i.e direct or indirect transition, is decided by the value of n [47]. Generally, if $n=1$ then it is direct transition and if $n=4$, then the transition become indirect [47]. The best fit for the $(\alpha h\nu)^2$ versus photon energy ($h\nu$) plot suggests a direct allowed transition in FeVO₄ and g-C₃N₄, which are consistent with the earlier literature reports [44,46]. The calculated band gap energies for g-C₃N₄, FeVO₄, and FeVCN 37 were 2.68, 1.77, and 1.98 eV, respectively (Fig. S6(a–c), ESI).

Materials were characterized by using FT-IR spectrometer. The absorption bands appeared in the range of 800–1700 cm⁻¹ (Fig. S7, ESI) can be assigned to the in-plane vibration of graphitic carbon nitride [46]. Further, the FT-IR peak at 807 cm⁻¹ corresponds to the out of plane bending vibration of triazine unit of the C–N heterocycles [35]. A strong terminal V–O stretching vibration frequency for VO₄ unit is observed at 990 cm⁻¹ in the FT-IR spectrum of FeVO₄. Two FT-IR bands at 652 cm⁻¹ and 830 cm⁻¹ are attributed to the mixed bridging of V–O–Fe stretching and bridging V–O–Fe stretching vibrations in FeVO₄ [40,45]. Broad absorption in the range of 3200–3500 cm⁻¹ is attributed to the presence of small amount of water present in the sample. Signature and position of FT-IR peaks clearly show the existence of g-C₃N₄ and FeVO₄ in all the FeVO₄/g-C₃N₄ nanocomposites.

Efficiency of a photocatalyst can be evaluated with the help of photoluminescence spectroscopy. Photoluminescence study provides information with reference to the charge separation, migration, and the extent of the recombination of photo generated charge carriers at the surface of photocatalyst. Intensity of photoluminescence spectrum is directly proportional to the recombination of photogenerated electron-hole pairs (Fig. 5b). The highest intensity of PL spectrum for g-C₃N₄ shows that the recombination of

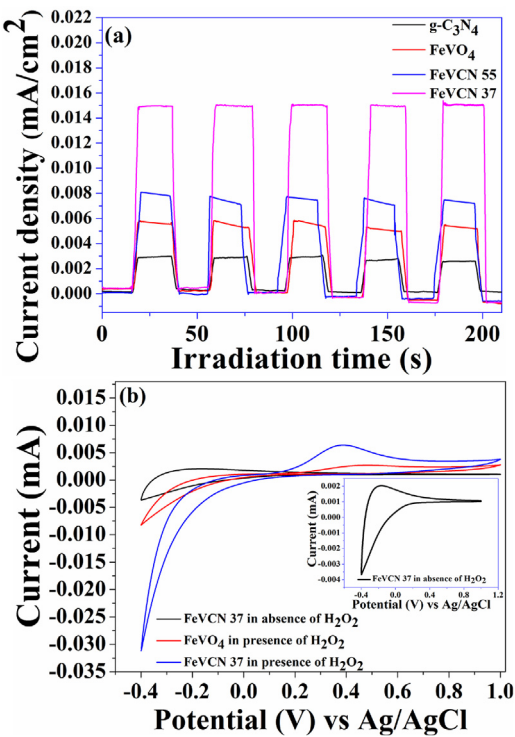


Fig. 6. (a) Transient photocurrent response (i-t) at FeVO₄, g-C₃N₄, FeVCN 37, and FeVCN 55 modified electrodes, and (b) cyclic voltammogram at FeVO₄ and FeVCN 37 modified electrodes.

charge carriers is the maximum among various materials investigated in this study. The intense reflection around 450 nm in g-C₃N₄ is attributed to the band to band PL transition of energy equal to the band gap energy of 2.7 eV [24]. FeVO₄ exhibits the lowest intense peak indicating the slowest recombination rate. With increase in the FeVO₄ content in the nanocomposites, PL intensity was decreased. Almost similar PL intensity was observed for FeVCN 37 and FeVCN 55. This investigation shows that the lowest recombination rate is not only the necessary condition for the catalyst to exhibit high activity. Low recombination rate along with optimum physico-chemical properties are required for the catalyst to exhibit excellent activity. The details are discussed in catalytic activity section of this manuscript.

Photoreactivity of the synthesized materials was also studied by photoelectrochemical measurements. Transient photocurrent (i-t) measurements were performed with g-C₃N₄, FeVO₄, FeVCN 37, and FeVCN 55 modified electrodes. Fig. 6(a) shows the (i-t) plots of different catalysts under dark and visible light illumination. Catalysts exhibited significant improvement in the response current after the visible light illumination. Intensity of the photocurrent response indicates the charge carrier (e⁻-h⁺) generation efficiency at the surface of the photocatalyst after visible light illumination [24]. Photogenerated electrons on the catalyst surface are mainly responsible for the generation of photocurrent. Upon visible light illumination, the light induced valence band electrons of the g-C₃N₄ get excited and migrated to the conduction band of FeVO₄. On the other hand, holes (h⁺) from the valence band of FeVO₄ shifted to the valence band of g-C₃N₄ leading to an effective overall charge carrier's separation resulting in the highest photocurrent generation in the nanocomposite FeVCN 37. The photocurrent response also indicates excellent photoelectrochemical reversibility under dark and illuminated condition. A sharp increment of the response current was observed upon visible light illumination which reverts back to the initial state under dark condition. Further, the photocurrent response recorded with FeVCN 37 was found to be three

times higher than g-C₃N₄ and four times higher than FeVO₄. The photocurrent response recorded with FeVCN 37 was found to be two times higher than FeVCN 55. All four photoelectrodes retained good reversibility and photostability of the active materials. The transient photocurrent response confirms that there is a strong interaction between the FeVO₄ and g-C₃N₄ in FeVCN 37, which is responsible for the generation of more numbers of charge carriers (high photocurrent response) with efficient charge-carrier separation, resulting in the high catalytic activity under photocatalytic condition.

X-ray photoelectron spectroscopy (XPS) is a very useful technique to verify the chemical constituents and the oxidation state of the elements present in the nanocomposite material. The surface survey XPS spectrum of FeVCN 37 catalyst is presented in Fig. 7(a), which confirms the presence of various elements (Fe, V, O, C, and N) in the FeVCN 37 nanocomposite. Fig. 7(b-f) shows the individual high resolution region XPS spectra for Fe 2p, V 2p, O 1s, C 1s, and N 1s energy level, respectively for FeVCN 37. The high resolution XPS spectrum for Fe 2p (Fig. 7(b)) exhibits two peaks at 710.7 and 724.8 eV that correspond to Fe2p_{1/2} and Fe2p_{3/2} binding energies of FeVO₄ [42]. The binding energy of Fe 2p doublets corresponds to the +3 oxidation state of Fe in the FeVO₄. Furthermore, two peaks at 515.3 and 524 eV are observed in the high resolution region spectrum of V 2p corresponding to the binding energies for V 2p_{1/2} and V 2p_{3/2}, respectively (Fig. 7(c)) in FeVO₄ [42]. The high resolution XPS spectrum for O 1s (Fig. 7(d)) shows two distinguished peaks at 528.4 and 530.1 eV that correspond to binding energies of O 1s and hydroxylated oxygen atom present in FeVO₄ [42]. The high resolution XPS spectrum of C 1s (Fig. 7(e)) exhibits two peaks at 284.6 and 288.1 eV that correspond to the SP² hybridized carbon atom and the carbon atom attached to three nitrogen atoms of g-C₃N₄ in FeVCN 37 nanocomposite [44]. Three different peaks for N 1s are observed in the high resolution XPS spectrum (Fig. 7(f)). The peak at 397.8 eV is due to nitrogen atom bonded to two carbon atom —C—N—C and the other two peaks at 399.1 and 400.1 eV are due to a tertiary nitrogen atom —N(C), and the nitrogen atom bonded to the surface hydrogen atom (—N—H), respectively [46,48]. Based on the results obtained from the XPS investigation it can be clearly concluded that nanocomposite of FeVO₄ and g-C₃N₄ was successfully synthesized.

3.2. Catalytic activity evaluation

Fe and V based inorganic materials are known for their oxidation capability. Fe based Fenton reagent is well known for the hydroxylation reaction. Similarly, V based catalysts have been investigated for the hydroxylation and oxidation reactions [49–54]. However, limited conversion and product selectivity always being the key issues associated with such catalyst. Researchers are developing various catalysts based on these metals for the hydroxylation and oxidation reactions that can be operated under mild reaction condition using an economical oxidant. In this study, three metal vanadates were prepared and their catalytic activities were evaluated in the oxidation and hydroxylation reactions. Thermal catalytic and photocatalytic activities of highly efficient metal vanadate and its nanocomposites with g-C₃N₄ were compared under optimum reaction condition.

3.3. Thermal catalytic activity

3.3.1. Aromatic hydroxylation under conventional thermal catalysis

3.3.1.1. *Influence of reaction parameters and kinetics investigation in benzene hydroxylation.* No reaction took place in the absence of catalyst (Table 2). FeVO₄ was chosen as a catalyst to optimize the reaction parameters. Solvent plays important role in the dis-

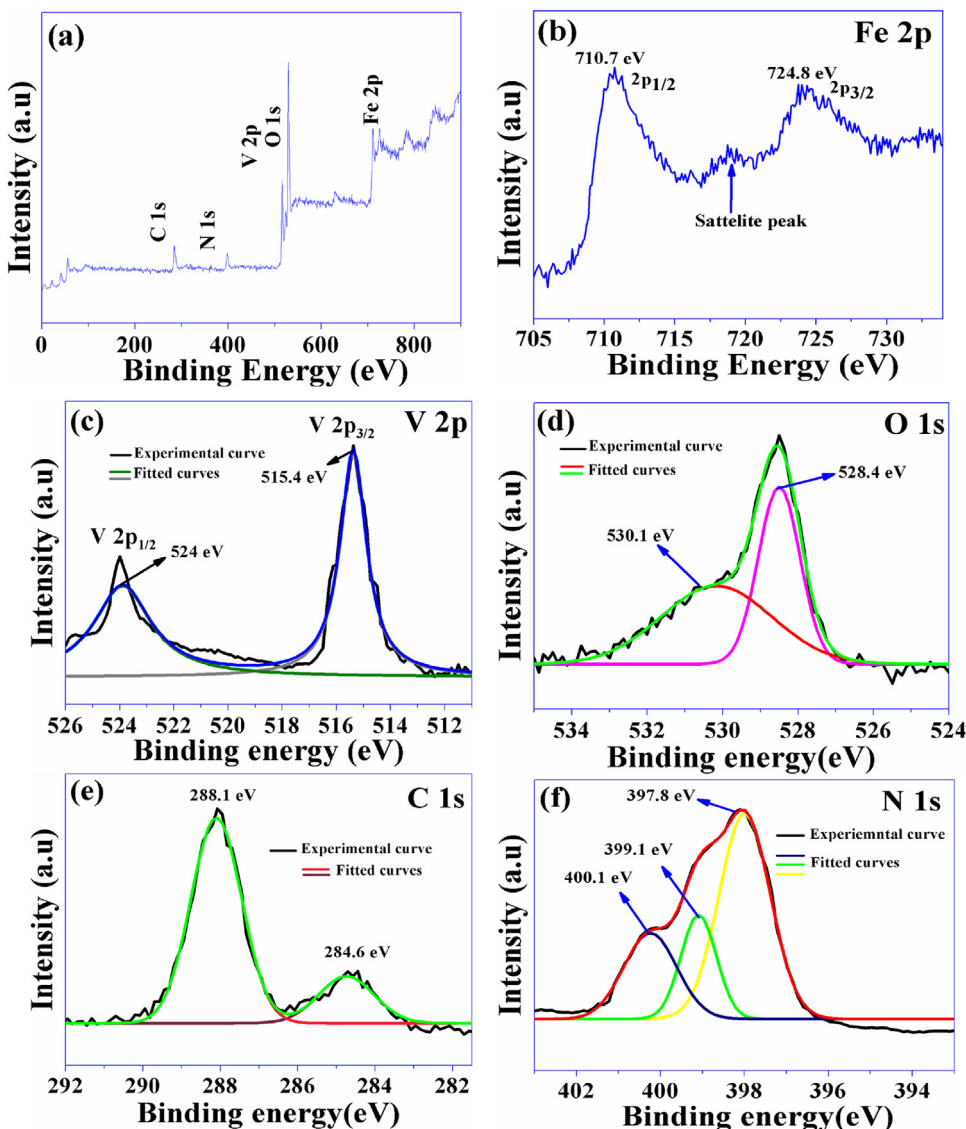


Fig. 7. (a) Surface survey XPS spectrum of FeVCN 37. High resolution XPS spectra of (b) Fe 2p, (c) V 2p, (d) O 1s, (e) C 1s, and (f) N 1s.

solution of reactant and transport of the reactant to the active sites of the catalyst (Table S1, ESI). Acetonitrile was found to be the best solvent among all the solvents investigated in this study. It may be noted that under the reaction condition, only phenol was obtained as a selective product. A detailed kinetic investigation was made to evaluate the dependence of various parameters such as substrate concentration, H_2O_2 concentration, catalyst concentration, and temperature on the rate of benzene hydroxylation reaction. Moreover, several thermodynamic parameters like activation energy (E_a), change in – Gibbs free energy of activation (ΔG), entropy of activation (ΔS), and free energy of enthalpy (ΔH) were calculated for this reaction. Furthermore, the active species involved in the benzene hydroxylation reaction was confirmed by the time-dependent UV-vis spectroscopy and radical scavenging experiments.

3.3.1.1. Influence of substrate concentration. Benzene hydroxylation was carried out at 60°C by varying the benzene concentration from 0.005 M – 0.02 M , while keeping H_2O_2 and catalyst concentration constant (Table S2a, ESI). With increase in the benzene concentration, benzene conversion was decreased. In order to determine the influence of benzene concentration on the rate of hydroxylation of benzene, rate was plotted versus benzene

concentration (Fig. 8(a)). It was found that the rate of hydroxylation of benzene to phenol exhibited a first order dependence with respect to the benzene concentration.

3.3.1.1.2. Influence of H_2O_2 (oxidant) concentration. Optimization showed that with increase in (H_2O_2 :benzene) ratio, catalytic activity increased and after (2.5:1), only a marginal increase in the catalytic activity was observed. Keeping the substrate, catalyst, and temperature constant (Table S2b, ESI), the H_2O_2 concentration was varied (0.01 M – 0.03 M). Plot of the rate of benzene hydroxylation (Fig. 8b) versus H_2O_2 was found to be linear which confirms the first order dependence with respect to oxidant concentration.

3.3.1.1.3. Influence of catalyst concentration. With increase in the amount of catalyst, conversion increased rapidly up to 50 mg of the catalyst. With further increase in the catalyst amount only a marginal increase in the catalytic activity was observed. Catalyst concentration was varied in between $3.5 \times 10^{-5}\text{ M}$ – $10.5 \times 10^{-5}\text{ M}$, (Table S2c) while keeping the other parameters constant. Fig. 8c shows the plot of rate of the benzene hydroxylation versus catalyst concentration. It can be seen from the graph that the rate of benzene hydroxylation is linear and exhibits a first-order dependency with respect to the catalyst concentration.

Table 2Liquid phase hydroxylation of benzene with H_2O_2 over various catalysts investigated in this study under different reaction condition.

Under conventional heating				
Entry No.	Catalyst	Benzene conversion (%)	Phenol selectivity (%)	H_2O_2 efficiency (%)
1.	None	0	–	–
2.	$g\text{-}C_3N_4$	1.2	100	<1
3.	$FeVO_4$	25.6	100	10.3
4.	$BiVO_4$	12.2	100	4.9
5.	$LaVO_4$	15.4	100	6.1
6.	V_2O_5	3.1	96.2	1.3
7.	FeVCN 19	14.8	96.8	6.1
8.	FeVCN 28	22.6	97.2	9.3
9.	FeVCN 37	30.5	98.1	12.4
10.	FeVCN 55	28.2	97.8	11.5
Under visible light				
11.	$g\text{-}C_3N_4$	0	0	0
12.	$FeVO_4$	30.4	100	12.2
13.	FeVCN 28	67.5	72.9 ($BQ=27.1$)	34.3
14.	FeVCN 37	93.8	62.7 ($BQ=37.3$)	54.9
15.	FeVCN 55	86.6	60.5 ($BQ=39.5$)	48.3

Reaction condition: Under thermal catalysis: Benzene (10 mmol), H_2O_2 (25 mmol), acetonitrile (6 mL), catalyst (50 mg), temp. (60 °C), time (4 h).Under photocatalysis: Benzene (10 mmol), H_2O_2 (25 mmol), acetonitrile (6 mL), catalyst (50 mg), temp. (25 °C), time (4 h). H_2O_2 eff (%) = 100 × ([Phenol]_s + 2[BQ]_s) / [H₂O₂]_{add}, where H_2O_2 eff is the effective conversion of H_2O_2 ; and [H₂O₂]_{add} is the molar concentration of H_2O_2 in the reaction mixture.

3.3.1.1.4. Influence of temperature. Temperature plays an important role in the hydroxylation reaction [51]. With the increase in the temperature from 30 °C to 60 °C, benzene conversion was increased but above 60 °C, the benzene conversion was decreased. This is due to the decomposition of H_2O_2 at elevated temperature [52]. Effect of temperature on the rate of hydroxylation of benzene to phenol was studied by varying the temperature between 30 °C and 60 °C (Table S2d) while keeping other parameters constant. From the Arrhenius plot of lnk versus $1/T$, the activation energy E_a was calculated (Fig. 8(d)). Arrhenius plot was used to determine the activation enthalpy ($\Delta H = E_a - RT$ at 60 °C). The free energy of the activation (ΔG) was determined using the equation: $\Delta G = -RT \ln(N_A h k / RT)$; where R is the gas constant, N_A is Avogadro number, h is the Planck's constant, k is the rate constant and T is the optimum reaction temperature, 60 °C [55]. Finally the activation of entropy was calculated using the formula: $\Delta S = (\Delta H - \Delta G) / T$. The values of E_a , ΔH , ΔG , and ΔS were calculated to be 16.42 kJ mol⁻¹, 13.65 kJ mol⁻¹, 3.53 kJ mol⁻¹, and 0.168 kJ mol⁻¹ °C⁻¹, respectively.

3.3.1.1.5. Influence of catalysts investigated in this study. After the evaluation of various reaction parameters, following reaction condition was optimized: benzene (10 mmol), H_2O_2 (25 mmol), catalyst (50 mg), acetonitrile (6 mL), temperature (60 °C), and time (4 h). After optimization of the reaction parameters, all the three vanadate catalysts were investigated (Table 2). $FeVO_4$ exhibited the best catalytic activity. Under the optimized reaction condition, V_2O_5 exhibited significantly low catalytic activity for the benzene hydroxylation reaction (Table 2). Furthermore, in this case in addition to phenol, p-benzoquinone was observed as a minor product. In order to increase the catalytic activity, nanocomposite materials based on $FeVO_4$ and $g\text{-}C_3N_4$ were prepared. Negligible catalytic activity was obtained with $g\text{-}C_3N_4$ itself (Table 2). With the increase in the content of $FeVO_4$ from 10% to 50% in the nanocomposites, catalytic activity was increased and reached maximum with 30% content (FeVCN 37) and then fell down with 50% $FeVO_4$ content in the nanocomposite (FeVCN 55) (Table 2). Less activity of FeVCN 55 when compared to FeVCN 37 can be correlated well with their physico-chemical properties, especially with textural properties (surface area of FeVCN 55 is less compared to FeVCN 37). In FeVCN 37, $FeVO_4$ was highly dispersed on the

surface of $g\text{-}C_3N_4$ and provided high surface area composite material. Highly dispersed and isolated $FeVO_4$ active sites in FeVCN 37 enhanced the adsorption of reactant and reactive species and facilitated the oxidation process. In these cases, phenol was obtained as a selective product but minor amount of p-benzoquinone was also obtained. Influence of the oxidant and H_2O_2 efficiency (Table 2) shows that only some fraction of H_2O_2 could be utilized in the reaction because H_2O_2 decomposed with time under the reaction condition. H_2O_2 efficiency was calculated by using the formula: H_2O_2 eff (%) = 100 × ([Phenol]_s + 2[BQ]_s) / [H₂O₂]_{add}, where H_2O_2 eff is the effective conversion of H_2O_2 ; and [H₂O₂]_{add} is the molar concentration of H_2O_2 in the reaction mixture [56]. Activity of FeVCN 37 was found to be better or similar when compared to various catalysts reported in the literature (Table S3).

3.3.1.1.6. Time dependent UV-vis study. Time dependent UV-vis study of the reaction mixture was performed in order to investigate the intermediates formed during the course of reaction. Under the optimum reaction condition, a fixed volume of the reaction mixture containing catalyst was diluted with acetonitrile and progress of the reaction was monitored by absorption spectroscopy at regular time intervals. Upon the addition of oxidant (H_2O_2) and substrate to the catalyst solution, the UV-vis spectrum shows the appearance of a new band in the range of 330–350 nm (Fig. S8(a), ESI). This new band is due to the formation of vanadium-peroxy species, which is an active intermediate species formed by the interaction of the vanadium centre (in the catalyst) and hydrogen peroxide. Similar type of vanadium-peroxy species has been reported in the literature for vanadium substituted heteropolymolybdates [57]. This band became more intense with the progress of the reaction (with increase in time). This increase in the intensity was an indication of phenol formation in the reaction mixture and probably due to the simultaneous H_2O_2 decomposition in the system [57]. Similar absorption spectra were obtained using FeVCN 19, FeVCN 28, and FeVCN 55 nanocatalysts (Fig. S8(b), ESI). Active intermediate species were formed in all the cases but their intensities were different. The most intense peak was obtained in FeVCN 37 which indicates the formation of more number of active species which resulted higher catalytic activity. This observation correlates well with the difference in the catalytic

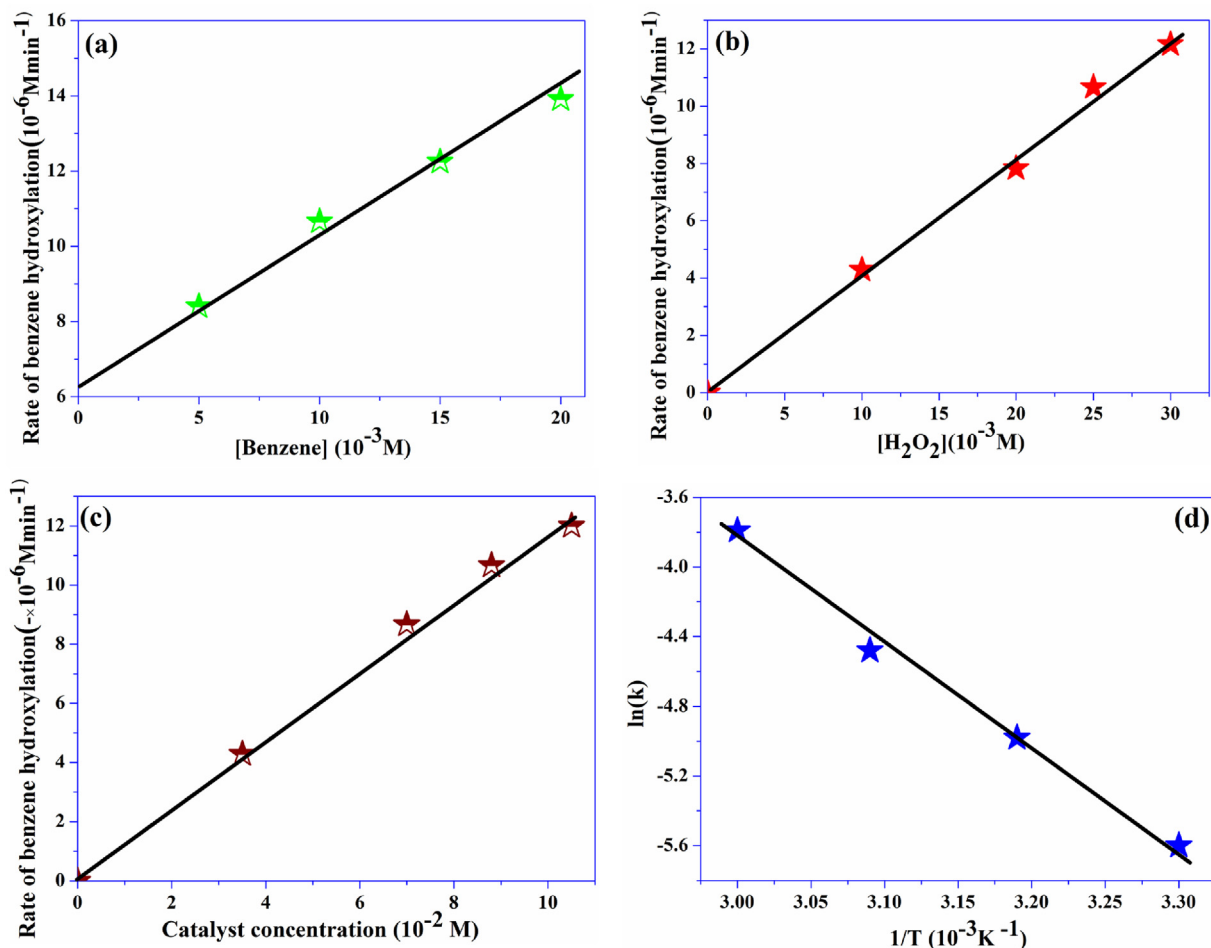


Fig. 8. (a) Effect of substrate concentration on the rate of benzene hydroxylation keeping other parameter constant, (b) Effect of H₂O₂ concentration on the rate of benzene hydroxylation keeping other parameter constant, (c) Effect of catalyst concentration on the rate of benzene hydroxylation keeping other parameter constant, (d) Effect of temperature concentration on the rate of benzene hydroxylation keeping other parameter constant, and Arrhenius plot.

activity observed in various nanocomposites investigated in this study. Further, this finding suggests that vanadium-peroxy species could be the main reactive intermediate for the hydroxylation of benzene (see mechanism, **Scheme 1**).

3.3.1.2. Hydroxylation of different aromatic compounds. Successful synthesis of phenol from benzene using H₂O₂ as oxidant motivated us to explore various aromatic compounds such as phenol, hydroquinone, naphthalene, and anthracene. In general, hydroxylation of phenol leads to the formation of three products, catechol (CA), hydroquinone (HQ) and p-benzoquinone (BQ). When the hydroxylation of phenol was carried out under the optimum reaction condition in the absence of catalyst, an extremely low phenol conversion was obtained (**Table 3**). Graphitic C₃N₄ and V₂O₅ exhibited a very low phenol conversion (**Table 3**). Using these catalysts, p-benzoquinone was obtained in very high selectivity. Only a minor amount of hydroquinone was obtained. All the metal vanadates were active and their activities were in the following order: FeVO₄> BiVO₄> LaVO₄. However, selectivity for p-benzoquinone in the case of BiVO₄ was marginally higher than FeVO₄. Although FeVO₄/g-C₃N₄ based nanocomposites exhibited more activity but the selectivity towards p-benzoquinone was marginally lower than FeVO₄ (**Table 3**). However in all the cases, selectivity for p-benzoquinone was more than 90%. With the increase in FeVO₄ content in the nanocomposites, phenol conversion was increased. The highest activity was obtained with FeVCN 37 (**Table 3**). In this case, H₂O₂ efficiency was calcu-

lated as: H₂O₂_{eff} (%) = 100 × ([Phenol]_s + [HQ]_s + 2[BQ]_s)/[H₂O₂]_{add}, where H₂O₂_{eff} is the effective conversion of H₂O₂; and [H₂O₂]_{add} is the molar concentration of H₂O₂ in the reaction mixture [56]. Under the optimized reaction condition, catalysts were investigated for the hydroxylation of hydroquinone. Using all these catalysts, p-benzoquinone was specifically obtained. In this case also, FeVCN 37 exhibited the highest activity among all the catalysts investigated in this study (**Table 3**). Various catalysts investigated in this study were also evaluated in the hydroxylation of naphthalene and anthracene. In this case also, only one product was specifically obtained (**Table 4**). The reactivity of the naphthalene hydroxylation was almost similar to that of the benzene hydroxylation but it produced only 1,4-naphthaquinone as a product (**Table 4**). The reactivity of the anthracene was significantly higher and produced only one product (9, 10-anthraquinone) using all the catalysts. In these cases also, FeVCN 37 exhibited the highest activity (**Table 4**). Such a high activity for anthracene hydroxylation is rarely reported in the literature (**Table 4**). It is important to note that only a few attempts have been made for the hydroxylation of anthracene in the past (**Table S4**). Activity of this catalyst was found to be better or similar when compared to various catalysts reported in the literature (**Table S4**).

3.3.1.3. Plausible mechanism of hydroxylation reaction. The activity of V₂O₅ was significantly low when compared to metal vanadates investigated in this study. Literature report suggests that, during the hydroxylation process, V⁵⁺ converts to V⁴⁺ after the reaction

Table 3Liquid phase hydroxylation of phenol and hydroquinone using H_2O_2 over various catalysts investigated in this study under different reaction condition.

Entry No	Catalyst	Phenol hydroxylation			Hydroquinone hydroxylation Benzoquinone yield. (%)	
		Phenol Conv. (%)	Selectivity (%)			
1.	None	2.1	1.2	98.8	<1	
2.	$g\text{-}C_3N_4$	6.3 (5.0) ^a	2.4	97.6	7.9 (6.3) ^a	
3.	V_2O_5	4.2 (3.3) ^a	3.5	96.5	26.6 (21.2) ^a	
4.	$FeVO_4$	36.2 (27.8) ^a	8.2	91.8	70.3 (56.2) ^a	
5.	$BiVO_4$	19.6 (15.3) ^a	5.2	94.8	41.2 (33.0) ^a	
6.	$LaVO_4$	23.4 (18.1) ^a	6.3	93.7	50.8 (40.6) ^a	
7.	FeVCN 19	16.4 (12.6) ^a	8.4	91.6	49.8 (39.9) ^a	
8.	FeVCN 28	30.5 (23.3) ^a	9.1	90.9	62.3 (49.9) ^a	
9.	FeVCN 37	46.6 (35.7) ^a	8.5	91.5	93.6 (74.9) ^a	
10.	FeVCN 55	40.5 (30.8) ^a	9.6	90.4	85.7 (68.6) ^a	
Under visible light						
11.	$g\text{-}C_3N_4$	0 (0) ^a	–	–	0	
12.	$FeVO_4$	40.8 (32.6) ^a	0	100	85.6 (68.5) ^a	
13.	FeVCN 28	41.9 (33.5) ^a	0	100	86.5 (69.2) ^a	
14.	FeVCN 37	58.7 (47.0) ^a	0	100	99.8 (79.9) ^a	
15.	FeVCN 55	53.5 (42.8) ^a	0	100	92.6 (74.1) ^a	

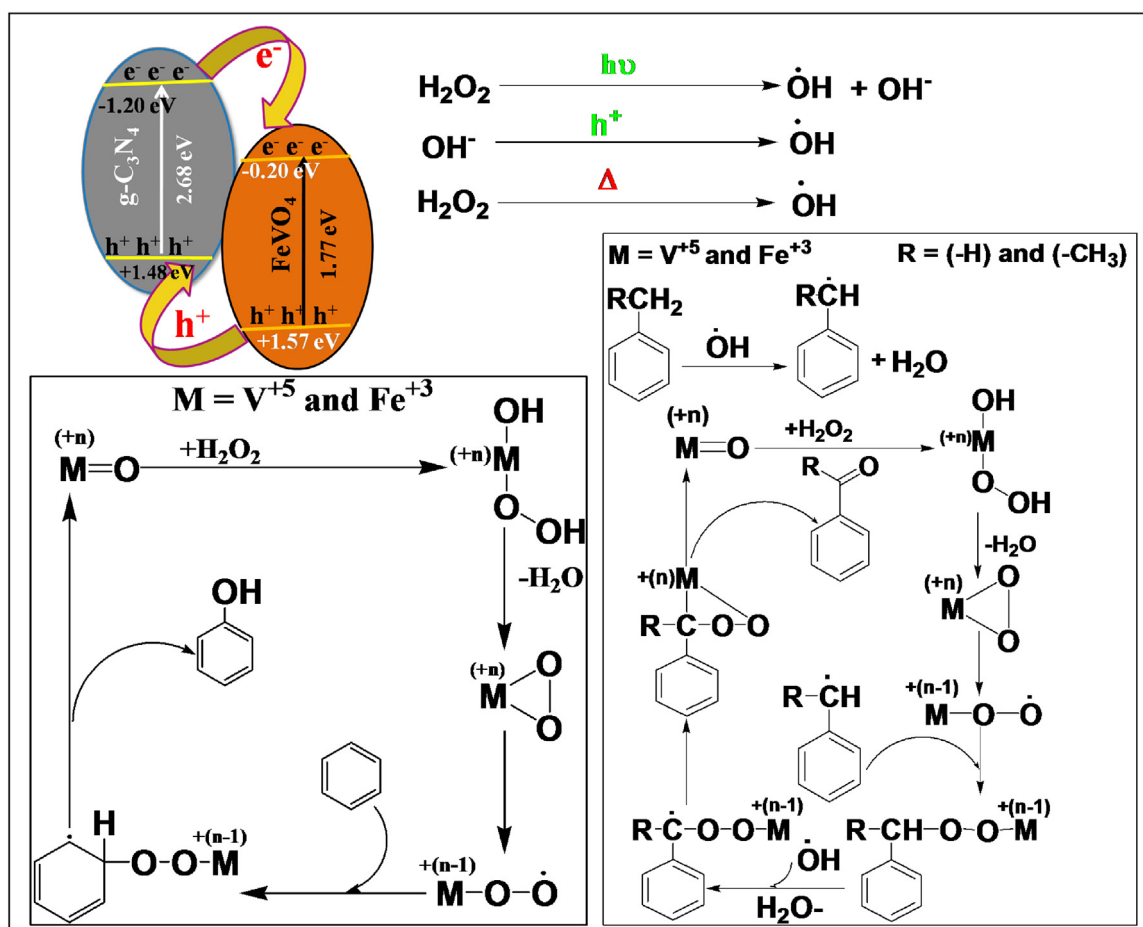
Reaction condition: Under thermal catalysis: Phenol/hydroquinone (10 mmol), H_2O_2 (25 mmol), acetonitrile (6 mL), catalyst (50 mg), temp. (60 °C), time (4 h). ^a H_2O_2 efficiency.Under photocatalysis: Phenol/hydroquinone (10 mmol), H_2O_2 (25 mmol), acetonitrile (6 mL), catalyst (50 mg), temp. (25 °C), time (4 h).^a H_2O_2 efficiency. $H_2O_{2\text{eff}}\% = 100 \times ([HQ]_s + 2[BQ]_s)/[H_2O_2]_{\text{add}}$, where $H_2O_{2\text{eff}}$ is the effective conversion of H_2O_2 ; and $[H_2O_2]_{\text{add}}$ is the molar concentration of H_2O_2 in the reaction mixture.**Table 4**Liquid phase hydroxylation of naphthalene and anthracene using H_2O_2 over various catalysts investigated in this study under different reaction condition.

Entry No.	Catalyst	1,4-Naphthaquinone yield (%)		H_2O_2 efficiency (%)	9, 10 Anthraquinone yield (%)	H_2O_2 efficiency (%)
		1,4-Naphthaquinone yield (%)	9, 10 Anthraquinone yield (%)			
1.	$g\text{-}C_3N_4$	<1	–	–	<1	–
2.	V_2O_5	4.8	3.2	3.8	3.2	2.6
3.	$FeVO_4$	20.2 (28.4) ^a	46.5 (52.7) ^a	16.1 (22.6) ^a	37.2 (42.2) ^a	17.0
4.	$BiVO_4$	9.2	21.3	7.4	30.4	24.3
5.	$LaVO_4$	12.6	47.8	10.0	66.3 (77.5) ^a	38.2
6.	FeVCN 19	12.8	66.3 (77.5) ^a	10.2	22.3 (55.3) ^a	53.0 (69.2) ^a
7.	FeVCN 28	19.2 (29.9) ^a	80.9 (99.2) ^a	15.3 (23.7) ^a	69.4 (86.3) ^a	71.2 (87.3) ^a
8.	FeVCN 37	27.9 (56.7) ^a	69.4 (86.3) ^a	22.3 (55.3) ^a	55.5 (75.4) ^a	–
9.	FeVCN 55	25.6 (50.2) ^a	–	20.4 (48.8) ^a	–	–

Reaction condition: Under thermal catalysis: Naphthalene/anthracene (10 mmol), H_2O_2 (25 mmol), acetonitrile (6 mL), catalyst (50 mg), temp. (60 °C), time (4 h).^a Reaction was performed under visible light using the same reaction condition but at 25 °C. $H_2O_{2\text{eff}}\% = 100 \times ([\text{Quinone}]_s)/[H_2O_2]_{\text{add}}$, where $H_2O_{2\text{eff}}$ is the effective conversion of H_2O_2 ; and $[H_2O_2]_{\text{add}}$ is the molar concentration of H_2O_2 in the reaction mixture.

with H_2O_2 and at the end of the reaction it restores V^{5+} state (Detail of the mechanism is discussed in the following section) [57]. Catalytic activity shows that the incorporation of another metal in the metal vanadate significantly changed its reactivity. By the incorporation of another metal atom, the redox property of V can be tailored which is responsible for the change in the reactivity. Fe, Bi, and La can switch their oxidation state between Fe^{2+} and Fe^{3+} , Bi^{4+} and Bi^{5+} , and La^{3+} to La^{5+} , respectively. Based on the catalytic activity data obtained, one can conclude that 'Fe' is the best suited metal

atom among all the three metals and can change the oxidation state of 'V' most effectively to impart high activity. Furthermore, it may be noted that Fe has the ability to exhibit the hydroxylation reaction [45,49]. In the hydroxylation process, Fe^{3+} converts to Fe^{2+} after the reaction with H_2O_2 and at the end of reaction it restores back to its original Fe^{3+} state [48]. Catalytic activity of $FeVO_4$ increased after it was dispersed on the external surface of $g\text{-}C_3N_4$. When $FeVO_4$ was loaded on the external surface of $g\text{-}C_3N_4$, active sites was highly dispersed and isolated when compared to the bulk $FeVO_4$. Such



Scheme 1. Plausible reaction pathways for benzene hydroxylation (left panel) and oxidation of toluene/ethyl benzene (right panel) under thermal catalytic and photocatalytic conditions.

isolated active sites exhibited higher activity when compared to the bulk FeVO_4 . Dispersion of FeVO_4 was optimum when the loading was 30%. Based on the catalytic activity data it can be concluded that 30% FeVO_4 loading over $\text{g-C}_3\text{N}_4$ was optimum to exhibit the highest activity.

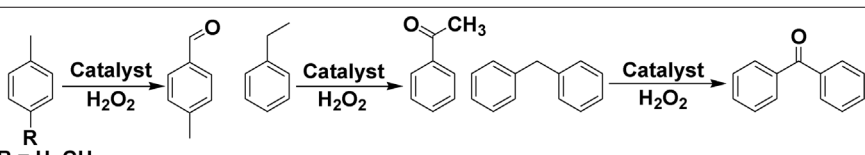
The plausible reaction mechanism for the benzene hydroxylation is presented in Scheme 1 (left side). In the first step, H_2O_2 chemisorbs on the active site of the catalyst (for example FeVCN 37). Active Fe and V species react with H_2O_2 and produce reactive peroxy-vanadate and peroxy-iron species. Formation of vanadium-peroxy species was confirmed using time dependent UV-vis study (see 3.2.1.1.6 section). Such species are reported when H_2O_2 reacts with V_2O_5 , and Fe/SBA-16 materials [53,57,58]. Strained three membered reactive species convert to other reactive VOO^\bullet and FeOO^\bullet radical species by the reduction of metal ($\text{V}^{4+}/\text{Fe}^{2+}$). In the next step, VOO^\bullet and FeOO^\bullet radical species abstract the proton ($\text{C}-\text{H}$) from the benzene (and other aromatic compounds) and form $\text{V}-\text{O}-\text{O}-\text{Ph}$ and $\text{Fe}-\text{O}-\text{O}-\text{Ph}$ species, which rearrange to give the product phenol and original $\text{V}^{5+}/\text{Fe}^{3+}$ species are regenerated. In order to validate the reactive free radical species, radical trapping experiment was carried out. Equivalent amounts of H_2O_2 and tertiary butyl alcohol (TBA) (which is known as a hydroxyl radical scavenger) were added into the reaction mixture under the optimum reaction condition for benzene hydroxylation [56]. Significantly low yield of the phenol was obtained (Fig. S9, ESI) in the presence of HO^\bullet scavenger, which clearly indicates that HO^\bullet plays an important role in the product formation.

3.3.2. Oxidation of aromatic compounds

Having found success in the hydroxylation reaction (Aromatic C–H activation), it was important to evaluate the activity of this catalyst in the oxidation of toluene, *p*-xylene, ethyl benzene, and diphenyl methane (Benzyllic C–H activation). It is important to note that the oxidation of toluene and ethyl benzene is very difficult. In most of the cases 2–5% conversion of toluene has been reported [59–62]. In this study, oxidation of toluene and ethyl benzene was performed at the similar reaction condition so that the comparison in the catalytic activity can be made. Under the optimum reaction condition, $\text{g-C}_3\text{N}_4$ and V_2O_5 both exhibited very low toluene conversion (~1%) (Table 5). Metal vanadates were more active than that of the $\text{g-C}_3\text{N}_4$ and V_2O_5 . Activity of metal vanadates followed the order: $\text{FeVO}_4 > \text{LaVO}_4 > \text{BiVO}_4$. However, in these cases also the toluene conversion was very low (~5%). Activity of the FeVO_4 was increased upon the dispersion of FeVO_4 on the $\text{g-C}_3\text{N}_4$ surface. Similar to the above catalytic investigation, in this case also FeVCN 37 exhibited the highest activity (Table 5). In all these cases, benzaldehyde was obtained as a product. When the similar reaction was performed with ethyl benzene, high reactivity of the catalyst was achieved. Catalytic reactivity order of various catalysts in the ethyl benzene oxidation was similar to that of the toluene oxidation. In this case also, only acetophenone was obtained as a product. Yield of the acetophenone was almost four folds higher in comparison to that of the benzaldehyde over highly active catalyst FeVCN 37 (Table 5). Activity of this catalyst was found to be better or similar when compared to various catalysts reported in the literature for toluene and ethyl benzene oxidation (Table S5 and Table S6). Acti-

Table 5

Liquid phase oxidation of toluene, *p*-xylene, ethyl benzene, and diphenyl methane using H_2O_2 over various catalysts investigated in this study under different reaction condition.

					
Under conventional heating					
Entry No.	Catalyst (%)	Benzaldehyde yield (%)	Acetophenone yield (%)	Benzophenone yield (%)	4-Methyl benzaldehyde Yield (%)
1.	–	–	<1	–	–
2.	$g\text{-C}_3\text{N}_4$	<1	1.3	–	–
3.	$V_2\text{O}_5$	1.2	5.8	–	–
4.	FeVO_4	5.6	21.6	20.4	11.2
5.	BiVO_4	2.1	9.3	–	–
6.	LaVO_4	2.8	14.7	–	–
7.	FeVCN 19	4.8	13.1	–	–
8.	FeVCN 28	8.1	21.9	–	–
9.	FeVCN 37	10.4	32.2	39.1	21.3
10.	FeVCN 55	8.2	27.6	–	–
Under visible light					
11.	$g\text{-C}_3\text{N}_4$	<1	–	–	–
12.	FeVO_4	13.6 ^a	–	–	–
13.	FeVCN 37	37.1 ^b	52.2 ^c	65.6	34.4

Reaction condition: Under thermal catalysis: Toluene/ethyl benzene/diphenyl methane/*p*-xylene (10 mmol), H_2O_2 (25 mmol), acetonitrile (6 mL), catalyst (50 mg), temp. (60 °C), time (4 h).

Under photocatalysis: Substrate (10 mmol), H_2O_2 (25 mmol), acetonitrile (6 mL), catalyst (50 mg), temp. (20–25 °C), time (4 h), 250 W high pressure visible lamp > 420 nm.

^a Toluene conversion = 33.7%, selectivity (Benzaldehyde = 40.3%, *o*-cresol = 32.7%, 4-methyl benzene 1,3-diol (27.0%).

^b Toluene conversion = 80%, selectivity (Benzaldehyde = 46.3%, *o*-cresol = 28.8%, 4-methyl benzene 1,3-diol (24.9%).

^c Ethylbenzene conversion = 91%, selectivity (Acetophenone = 57.4%, 2-hydroxy ethyl benzene = 20.2%, 1-Phenylethanol (22.4%).

vated substrate such as *p*-xylene and diphenyl methane produced better activity (almost twice) when compared to toluene and ethyl benzene, respectively. Oxidation of *p*-xylene and diphenyl methane produced 4-methyl benzaldehyde and benzophenone as specific products, respectively.

The plausible reaction mechanism for the toluene/ethyl benzene oxidation is presented in **Scheme 1** (right panel). Reaction proceeds through similar reactive species as it is shown for benzene hydroxylation in **Scheme 1** (left panel). In this case, H_2O_2 has two roles to play. H_2O_2 thermally decomposes and generates HO^\bullet radicals, which react with toluene/ethyl benzene to form radical species. These radical species further react with VOO^\bullet and FeOO^\bullet (as discussed in the proposed mechanism in **Scheme 1** (left panel)) and form $\text{V}/\text{Fe}-\text{O}-\text{O}-\text{CH}_2\text{Ph}/-\text{CH}_3\text{CHPh}$ species, which rearrange to give benzaldehyde/acetophenone and original $\text{V}^{5+}/\text{Fe}^{3+}$ species are regenerated. In order to validate the reactive species catalyzing these reactions, radical trapping experiments were performed. Equivalent amounts of TBA and H_2O_2 were added into the reaction mixture under the optimum reaction condition for toluene and ethyl benzene oxidation reactions. Significantly low yield of the product was obtained (Fig. S9, ESI) in the presence of HO^\bullet scavenger, which clearly indicates that HO^\bullet plays dominant role in the product formation.

3.4. Visible light photocatalysis

In this study photocatalytic reactions were performed at the same set of reaction condition to that of conventional thermal catalysis without external heating. The photocatalytic reactions were performed at ambient temperature (24–25 °C). Graphitic C_3N_4 was inactive under the optimum reaction condition for the hydroxylation of aromatic compounds. FeVO_4 exhibited somewhat better activity under visible light in phenol hydroxylation when compared to the thermal catalysis (**Table 2**). Significantly high benzene conversion and H_2O_2 efficiency were obtained with FeVCN 37

(**Table 2**). In this case, in addition to phenol, *p*-benzoquinone was also obtained which signifies the high activity of FeVCN 37 under visible light. Similar trend in the enhancement of the activity was obtained in the hydroxylation of other aromatic compounds (phenol, naphthalene, and anthracene) over FeVO_4 , FeVCN 28, FeVCN 37, and FeVCN 55 investigated in this study under visible light condition (**Table 3** and **Table 4**). Improvement in the desired product yield was obtained for benzylic $-\text{C}-\text{H}$ activation. It may be noted that during thermal catalysis, only aliphatic $\text{C}-\text{H}$ activation took place during the oxidation of toluene and afforded benzaldehyde as a product with low yield. Under the visible light condition, aliphatic as well as aromatic $\text{C}-\text{H}$ activation took place which afforded three products benzaldehyde (aliphatic $\text{C}-\text{H}$ activated product, Selec. = 46.3%), *o*-cresol and 4-methyl benzene 1,3-diol (aromatic $\text{C}-\text{H}$ activated products, Selec. = 53.7%) (**Table 5**). Under visible light condition, it afforded three times higher yield of benzaldehyde when compared to thermal catalysis. In the case of ethyl benzene also both aromatic and aliphatic $\text{C}-\text{H}$ activation took place (**Table 5**). Under visible light condition, 1.6 times higher acetophenone yield was obtained when compared to thermal catalysis. However, in the case of diphenyl methane and *p*-xylene, only aliphatic $\text{C}-\text{H}$ activated products were obtained in high yields under visible light condition (**Table 5**). Under photocatalytic condition also, catalytic activity was increased with increase in the content of FeVO_4 and reached maxima with 30% content (FeVCN 37) and then fell down with 50% FeVO_4 content in the nanocomposite (FeVCN 55) (**Tables 2–4**). Less activity of FeVCN 55 when compared to FeVCN 37 can be correlated well with their physico-chemical properties (especially with textural properties (surface area of FeVCN 55 is less compared to FeVCN 37)) and photophysical processes (excellent photoluminescence response (similar intence photoluminescence spectra of FeVCN 37 and FeVCN 55), and photocurrent response (higher photocurrent response for FeVCN 37 when compared to FeVCN 55)). Based on the results obtained it can be concluded that the H_2O_2 efficiency, reactant conversion, and

yield of the products obtained under visible light condition were much better when compared to the reactions took place under conventional thermal catalysis.

During the thermal catalytic process, diffusion, adsorption, reaction, and desorption are fundamental steps involved. In a photocatalytic process, reactants are generally strongly adsorbed at the catalyst surface (physical adsorption) due to the low operating temperature. It is followed by several photochemical reactions and physical processes (such as photoadsorption and photodesorption) which are activated by light. Due to the strong adsorption of reactants and efficient activation of aliphatic and aromatic C–H bonds by light, multiple products were obtained in the oxidation of aromatic compounds such as toluene and ethyl benzene. Reaction did not take place in the dark condition or in the absence of photocatalyst at the optimum reaction condition. When the similar reaction was performed using $\text{g-C}_3\text{N}_4$, no reaction took place. Though $\text{g-C}_3\text{N}_4$ has ability to absorb visible light but it was unable to give any oxidation product. This provides evidence that catalytic active species was FeVO_4 . FeVO_4 exhibited good activity because of its catalytic action and visible light absorption efficiency. Based on the PL investigation one can anticipate that FeVO_4 should have exhibited better activity. However, catalytic results showed that FeVCN 37 exhibited more activity than FeVO_4 . This provides evidence that efficient charge separation is not only the desired criteria for the catalyst to exhibit the high activity. In FeVCN 37, FeVO_4 was highly dispersed on the surface of $\text{g-C}_3\text{N}_4$ and provided high surface area composite materials. Highly dispersed and isolated FeVO_4 active sites in FeVCN 37 enhanced the adsorption of reactant and reactive species and facilitated the oxidation process. FeVCN 37 exhibited the highest photoresponse current which shows the highest charge carrier ($\text{e}^-\text{-h}^+$) generation efficiency at the surface of the photocatalyst. These charge carriers are responsible for the generation of large numbers of reactive HO^\bullet species under visible light condition that enabled high catalytic activity. Therefore, the combination of physical adsorption and photophysical processes (photoadsorption, photodesorption, efficient charge separation, and photocurrent response) are important for the activation of aromatic and benzylic C–H bonds to oxygenated products. After the light absorption, electrons are generated and migrated to the conduction band of the catalyst, where they react with H_2O_2 to form HO^\bullet . Upon absorption of light, photogenerated electrons react with H_2O_2 to form HO^\bullet and OH^- and then hole finally reacts with OH^- to produce HO^\bullet ($\text{H}_2\text{O}_2 + \text{e}^- \rightarrow \text{HO}^\bullet + \text{OH}^-$; $\text{h}^+ + \text{OH}^- \rightarrow \text{HO}^\bullet$). OH^- can be easily converted to HO^\bullet at FeVO_4 due to its favorable redox potential ($\text{OH}^-/\text{HO}^\bullet = 1.99 \text{ eV}$) [24]. The photogenerated HO^\bullet are responsible for the oxidation of aromatic compounds investigated in this study by following the same sequence of reactions as shown in the conventional thermal catalysis (Scheme 1).

High H_2O_2 efficiency and involvement of HO^\bullet can be confirmed from the fluorescence study using terephthalic acid (TA) as a probe molecule [63]. The amount of available HO^\bullet was estimated by measuring the amount of TAOH, which was formed by the reaction of HO^\bullet with TA. The photocatalyst FeVCN 37 decomposes H_2O_2 and generates HO^\bullet radicals which are the main active species in all these reactions. Two kinds of HO^\bullet are suggested in the literature; the adsorbed HO^\bullet and the free HO^\bullet . It has been reported that trapped hole is equivalent to the adsorbed HO^\bullet and the redox potential of this process is 1.5 V [64]. Whereas, the redox potential of free HO^\bullet is 1.9 V [65]. Through fluorescence study using TA, it can be proved that TA reacts with free HO^\bullet and it cannot react with the adsorbed HO^\bullet . Fluorescence study using TA was performed under three conditions: visible light irradiation, under dark condition at ambient temperature, and under conventional thermal condition at 60 °C (Fig. 9(b)). Under the visible light condition, as the reaction was progressed, the concentration of TAOH was increased and then remained constant after 4 h. This experiment suggests that with

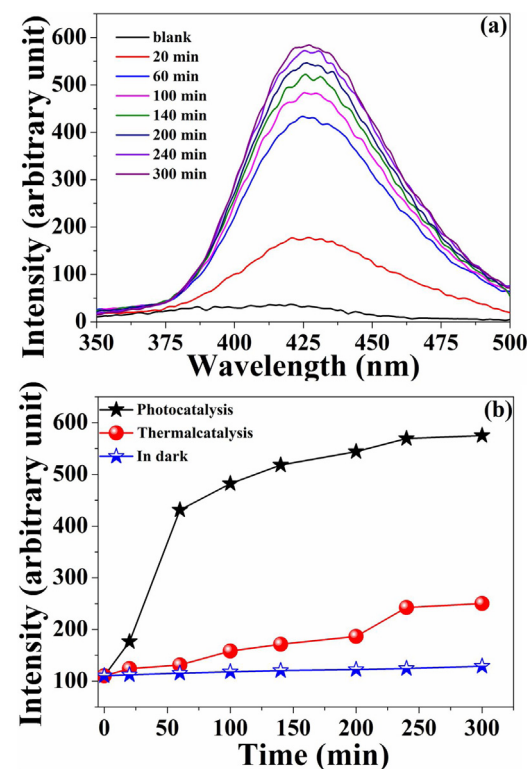


Fig. 9. (a) Fluorescence study for HO^\bullet radical trapping experiment under visible light illumination at different time intervals. (b) Intensity of the hydroxyl radical bind terephthalic acid vs time under different reaction conditions.

progress of the reaction, HO^\bullet was formed and reacted with TA to form TAOH during first 4 h. By the end of 4 h, almost all H_2O_2 was consumed, therefore no further HO^\bullet was generated and thereby no increase in the concentration of TAOH was observed. Negligible TAOH was observed which confirmed that HO^\bullet was not produced in dark condition. Significant difference in the fluorescence intensity of TAOH under light irradiation and conventional thermal condition correlates well with the high reactivity and H_2O_2 efficiency shown in Table 2-5. Under conventional thermal condition, HO^\bullet was formed but it decomposed quickly or adsorbed at the surface, therefore it was unavailable to react with TA to form TAOH. Furthermore, reactions were also performed with equivalent amounts of tertiary butyl alcohol and H_2O_2 under the optimum reaction condition for toluene and ethyl benzene. Significantly low yield of the product was obtained (Fig. S9, ESI) in the presence of HO^\bullet scavenger, which clearly indicates that HO^\bullet plays dominant role in the visible light assisted oxidation of aromatic compounds. Catalytic activity data, physico-chemical characterizations, and faster H_2O_2 decomposition clearly show that there is an excellent structure-activity relationship, which facilitates the separation and migration of charge carriers that are responsible for the formation of active HO^\bullet species that react with various aromatic compounds to form oxygenated products.

Furthermore, the involvement of the active radical species was also confirmed with the help of cyclic voltammetry (CV). Fig. 6(b) shows that no oxidation peak was observed in the absence of H_2O_2 at FeVCN 37 modified electrode. After the addition of H_2O_2 , an oxidation peak at 0.32 V was observed, this indicates that H_2O_2 decomposition had taken place at the electrode surface. An oxidation peak at higher potential (0.40 V) was observed at FeVO_4 modified electrode. Sharp oxidation peak and low onset potential enable it towards a faster decomposition due to the lower activation energy for the $\text{H}_2\text{O}_2/\text{HO}^\bullet$ decomposition at FeVCN 37 modified electrode when compared to FeVO_4 modified electrode [30]. Based

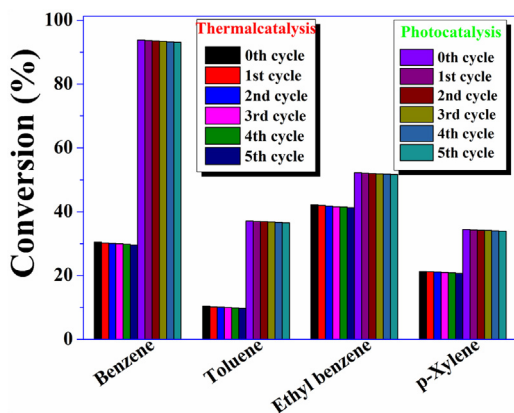


Fig. 10. Catalytic recyclability up to 5 recycles for FeVCN 37 in the hydroxylation and oxidation reactions carried out in this study.

on the results obtained it can be concluded that H_2O_2 was easily decomposed to HO^\bullet in the presence of FeVCN 37 that reacted with reactant and produced oxidation products in higher yield when compared to FeVO_4 . These results are in consistent with the results obtained from the fluorescence study.

3.5. Stability and recyclability

Stability and recyclability of the catalyst was investigated. Catalyst was separated from the reaction mixture and used in the next cycle. One of the important features of this catalytic process is that the catalyst was magnetically separable (Fig. S11, ESI) and easily recoverable from the reaction mixture. This is one of the most important features of the sustainable fine chemical synthesis. Recycling study (up to five recycles) was performed for the hydroxylation of benzene & phenol and oxidation of toluene & ethyl benzene, using highly active catalyst FeVCN 37 under conventional thermal catalytic and photocatalytic conditions. After each reaction, catalyst was magnetically separated (Fig. S10, ESI), washed with acetonitrile, dried at 100 °C for 10 h and then used in the next cycle. Results obtained during the recycling of the catalyst are presented with respect to conversion of the reactant (Fig. 10). XRD pattern, SEM micrograph, EDX elemental mapping, and XPS spectrum of the recovered FeVCN 37 catalyst obtained under conventional thermal catalysis are presented (ESI). Based on the catalytic results obtained, it may be concluded that catalyst was stable and exhibited negligible loss in the activity even after five recycles (Fig. 10). XRD analysis of the recovered catalyst showed that material exhibited no phase transformation or loss in the crystallinity after reuse (Fig. S11, ESI). N_2 -adsorption investigation showed that only a marginal change in the textural properties was observed for the reused catalyst (Table 1). EDX elemental mapping confirmed the presence of various constituent elements present in the recovered catalyst (Fig. S12, ESI). Surface survey XPS spectrum of the recycled catalyst was very similar to that of the fresh catalyst, which confirmed that no appreciable change in the chemical constituents and the oxidation state of various elements present in the recovered catalyst took place while it was recycled (Fig. S13, ESI).

4. Conclusions

Nanocomposites of FeVO_4 and $\text{g-C}_3\text{N}_4$ with different compositions were synthesized by a simple annealing method. Physico-chemical characterizations revealed that 15–20 nm FeVO_4 nanoparticles were supported and finely dispersed on $\text{g-C}_3\text{N}_4$ that exhibited better textural properties compared to parent FeVO_4 and

$\text{g-C}_3\text{N}_4$ materials. Catalytic investigations show that FeVO_4 exhibited the highest activity among the metal vanadates investigated in this study. Furthermore, nanocomposite of FeVO_4 and $\text{g-C}_3\text{N}_4$ with 30% loading of FeVO_4 exhibited the highest activity in the liquid phase (thermal catalytic/photocatalytic) oxidation of wide range aromatic compounds such as benzene, phenol, hydroquinone, naphthalene, anthracene, toluene, ethyl benzene, p-xylene, and diphenyl methane. Kinetic investigation under conventional thermal catalysis showed that the rate of benzene hydroxylation was first order with respect to H_2O_2 and benzene concentration with the activation energy (E_a) of 16.42 kJ M^{-1} . Time dependent UV-vis study showed that vanadium-peroxy was the active species for this reaction. It also provided evidence for the generation of more number of active species using the nanocomposite of FeVO_4 and $\text{g-C}_3\text{N}_4$ with 30% loading of FeVO_4 when compared to other nanocomposites prepared in this study. Nanocomposite catalyst exhibited significantly higher activity under visible light condition when compared to conventional thermal catalysis. Using this catalyst reasonably good product yields were obtained when compared to various catalysts reported in the literature. Fluorescence and radical trapping experiments confirmed that in-situ formed hydroxyl radicals were responsible for the oxidation of these aromatic compounds that leads to form wide variety of commercially important fine chemicals. Significant difference in the fluorescence intensity of TAOH under visible light irradiation and conventional thermal condition correlated well with the high catalytic activity and H_2O_2 efficiency under visible light condition. Significantly low yield of the product was obtained in the presence of HO^\bullet scavenger, which confirmed that HO^\bullet plays dominant role in the oxidation of aromatic compounds. Highly dispersed and isolated FeVO_4 active sites in nanocomposites enhanced the adsorption of reactant and reactive species and facilitated the oxidation process. Nanocomposite of FeVO_4 and $\text{g-C}_3\text{N}_4$ with 30% loading of FeVO_4 exhibited the highest photocurrent response which showed the highest charge carrier ($e^- - h^+$) generation efficiency at the surface of the photocatalyst. These charge carriers are responsible for the generation of large numbers of reactive HO^\bullet species under visible light condition that enabled high catalytic activity. Ease of magnetic separation of the catalyst and recyclability up to five recycles with negligible loss in the catalytic activity are other interesting features of this catalytic process. We envisaged here that dual metal catalysis by Fe^{+3} & V^{+5} , optimum dispersion of FeVO_4 nanospheres on $\text{g-C}_3\text{N}_4$ matrix, optimum textural properties, and optimum photo physical processes (photoadsorption, photodesorption, efficient charge separation, and photoreaction current) are responsible for the superior catalytic activity of nanocomposite of FeVO_4 and $\text{g-C}_3\text{N}_4$ with 30% loading of FeVO_4 under visible light condition. Simple synthetic procedure, high catalytic activity, selectivity, eco-friendliness of the catalytic process involving H_2O_2 , easy recovery by a magnet, and efficient recyclability of the catalyst are some of the attractive key features of this sustainable catalytic process. We believe that such a systematic comparative study (thermal catalysis vs photocatalysis) under one umbrella will encourage scientific community to develop suitable catalyst for an appointed catalytic reaction.

Acknowledgements

Authors are thankful to Nano Mission, Department of Science and Technology, New Delhi (SR/NM/NS-1054/2015) for financial support. SS acknowledge financial assistance to MHRD, New Delhi. Authors are thankful to SAIF, IIT Bombay for HRTEM analysis. Authors are also thankful to DST-FIST funded XPS facility at Department of Physics, IIT Kharagpur.

Appendix A. Supplementary data

Supplementary data associated with this article can be found, in the online version, at <http://dx.doi.org/10.1016/j.apcatb.2017.06.043>.

References

- [1] F. Lobermann, P. Mayer, D. Trauner, Biomimetic synthesis of (\leftarrow -)pycnanthuquinone C through the Diels-Alder reaction of a vinyl quinone, *Angew. Chem. Int. Ed.* 49 (2010) 6199–6202.
- [2] M. Kawamukai, Bioproduction and novel roles of ubiquinone, *J. Biosci. Bioeng.* 94 (2002) 511–517.
- [3] K.C. Nicolaou, S.A. Snyder, T. Montagnon, G. Vassilikogiannakis, The Diels-Alder reaction in total synthesis, *Angew. Chem. Int. Ed.* 41 (2002) 1668–1698.
- [4] K. Weissermel, H.-J. Arpe, *Industrial Organic Chemistry*, vol. 354, 3rd edition, VCH Publishers, New York, 1997.
- [5] K.T.V. Rao, P.S.N. Rao, P. Nagaraju, P.S.S. Prasad, N. Lingaiah, Room temperature selective oxidation of toluene over vanadium substituted polyoxometalate catalysts, *J. Mol. Catal. A: Chem.* 303 (2009) 84–89.
- [6] A. Martin, U. Bentrup, G.-U. Wolf, The effect of alkali metal promotion on vanadium-containing catalysts in the vapour phase oxidation of methyl aromatics to the corresponding aldehydes, *Appl. Catal. A* 227 (2002) 131–142.
- [7] H.L. Han, G.D. Ding, T.B. Wu, D.X. Yang, T. Jiang, B.X. Han, Cu and boron doped carbon nitride for highly selective oxidation of toluene to benzaldehyde, *Molecules* 20 (2015) 12686–12697.
- [8] W. Partenheimer, Methodology and scope of metal/bromide autoxidation of hydrocarbons, *Catal. Today* 23 (1995) 69–158.
- [9] M.G. Egusquiza, G.P. Romanelli, C.I. Cabello, I.L. Botto, H.J. Thomas, Arene and phenol oxidation with hydrogen peroxide using 'sandwich' type substituted polyoxometalates as catalysts, *Catal. Commun.* 9 (2008) 45–50.
- [10] A.-M. Abu-Elfotoh, K. Tsuzuki, T.B. Nguyen, S. Chanthamath, K. Shibatomi, S. Iwasa, Quinones synthesis via hydrogen peroxide oxidation of dihydroxy arenes catalyzed by homogeneous and macroporous-polymer-supported ruthenium catalysts, *Tetrahedron* 69 (2013) 8612–8617.
- [11] D. Barbera, F. Cavani, T. D'Alessandro, G. Fornasari, S. Guidetti, A. Aloise, G. Giordano, M. Piumetti, B. Bonelli, C. Zanzottera, The control of selectivity in benzene hydroxylation catalyzed by TS-1: The solvent effect and the role of crystallite size, *J. Catal.* 275 (2010) 158–169.
- [12] P. Ratnasamy, D. Srinivas, H. Knözinger, Active sites and reactive intermediates in titanium silicate molecular sieves, *Adv. Catal.* 48 (2004) 1, Academic Press.
- [13] K. Na, C. Jo, J. Kim, W.-S. Ahn, R. Ryoo, Titanosilicate nanosheets with single-unit cell thickness as an oxidation catalyst using peroxides, *ACS Catal.* (2011) 901–907.
- [14] R. Kore, R. Srivastava, B. Satpati, Highly efficient nanocrystalline zirconiosilicate catalysts for the aminolysis, alcoholysis, and hydroamination reactions, *ACS Catal.* 3 (2013) 2891–2904.
- [15] B. Sarmah, R. Srivastava, B. Satpati, 1; Highly efficient silver nanoparticles supported nanocrystalline zirconiosilicate catalyst for the epoxidation and hydration reactions, *Chem. Sel.* 1 (2016) 1047–1056.
- [16] B. Li, N. Wu, K. Wu, J. Liu, C. Han, X. Li, V. Bimetallic, Ti incorporated MCM-[41;1] molecular sieves and their catalytic properties, *RSC Adv.* 5 (2015) 16598–16603.
- [17] N.A. Alekar, V. Indira, S.B. Halligudi, D. Srinivas, S. Gopinathan, C. Gopinathan, Kinetics and mechanism of selective hydroxylation of benzene catalysed by vanadium substituted heteropolymolybdates, *J. Mol. Catal. A: Chem.* 164 (2000) 181–189.
- [18] R.K. Jha, S. Shylesh, S.S. Bhoware, A.P. Singh, Oxidation of ethyl benzene and diphenyl methane over ordered mesoporous M-MCM-41 (M = Ti, V, Cr). Synthesis, characterization and structure-activity correlations, *Microporous Mesoporous Mat.* 95 (2006) 154–163.
- [19] D. Habibi, A.R. Faraji, M. Arshadi, J.L.G. Fierro, Characterization and catalytic activity of a novel Fe nano-catalyst as efficient heterogeneous catalyst for selective oxidation of ethylbenzene, cyclohexene, and benzylalcohol, *J. Mol. Catal. A: Chem.* 372 (2013) 90–99.
- [20] D. Baykan, N.A. Oztas, Synthesis of iron orthophosphate catalysts by solution and solution combustion methods for the hydroxylation of benzene to phenol, *Mater. Res. Bull.* 64 (2015) 294–300.
- [21] L. Li, Q. Meng, J. Wen, J. Wang, G. Tu, C. Xu, F. Zhang, Y. Zhong, W. Zhu, Q. Xiao, Improved performance of hierarchical Fe-ZSM-5 in the direct oxidation of benzene to phenol by N_2O , *Microporous Mesoporous Mat.* 227 (2016) 252–257.
- [22] D. Yang, T. Jiang, T. Wu, P. Zhang, H. Han, B. Han, Highly selective oxidation of cyclohexene to 2-cyclohexene-1-one in water using molecular oxygen over Fe-Co-g-C₃N₄, *Catal. Sci. Technol.* 6 (2016) 193–200.
- [23] J. Liu, H.Q. Wang, M. Antonietti, Graphitic carbon nitride reloaded: emerging applications beyond (photo)catalysis, *Chem. Soc. Rev.* 45 (2016) 2308–2326.
- [24] S. Samanta, S. Khilari, D. Pradhan, R. Srivastava, Visible light driven, selective oxidation of aromatic alcohols and amines with O_2 using BiVO₄/g-C₃N₄ nanocomposite: a systematic and comprehensive study towards the development of photocatalytic process, *ACS Sustain. Chem. Eng.* 5 (2017) 2562–2577.
- [25] Y. Gong, M. Li, H. Li, Y. Wang, Graphitic carbon nitride polymers: promising catalysts or catalyst supports for heterogeneous oxidation and hydrogenation, *Green Chem.* 17 (2015) 715–736.
- [26] L. Zhou, H. Zhang, H. Sun, S. Liu, M.O. Tade, S. Wang, W. Jin, Recent advances in non-metal modification of graphitic carbon nitride for photocatalysis: a historic review, *Catal. Sci. Technol.* 6 (2016) 7002–7023.
- [27] S. Patnaik, S. Martha, S. Acharya, K.M. Parida, An overview of the modification of g-C₃N₄ with high carbon containing materials for photocatalytic applications, *Inorg. Chem. Front.* 3 (2016) 336–347.
- [28] K.S. Lakhi, D.H. Park, K. Al-Bhaily, W. Cha, B. Viswanathan, J.H. Choy, A. Vinu, Mesoporous carbon nitrides: synthesis, functionalization, and applications, *Chem. Soc. Rev.* 46 (2017) 72–101.
- [29] X. Dong, F. Cheng, Recent development in exfoliated two-dimensional g-C₃N₄ nanosheets for photocatalytic applications, *J. Mater. Chem. A* 3 (2015) 23642–23652.
- [30] X. Chen, J. Zhang, X. Fu, M. Antonietti, X. Wang, Fe-g-C₃N₄-Catalyzed oxidation of benzene to phenol using hydrogen peroxide and visible light, *J. Am. Chem. Soc.* 131 (2009) 11658–11659.
- [31] S. Verma, N.R.B. Baig, M.N. Nadagouda, R.S. Varma, Photocatalytic C-H activation of hydrocarbons over VO@g-C₃N₄, *ACS Sustain. Chem. Eng.* 4 (2016) 2333–2336.
- [32] J. Zhang, Y. Nosaka, Mechanism of the OH radical generation in photocatalysis with TiO₂ of different crystalline types, *J. Phys. Chem. C* 118 (2014) 10824–10832.
- [33] Y. Nosaka, A. Nosaka, Understanding hydroxyl radical (OH) generation processes in photocatalysis, *ACS Energy Lett.* 1 (2016) 356–359.
- [34] K. Sahel, L. Elsellami, I. Mirali, F. Dappozze, M. Bouhent, C. Guillard, Hydrogen peroxide and photocatalysis, *Appl. Catal. B* 188 (2016) 106–112.
- [35] M. Wang, G. Fang, P. Liu, D. Zhou, C. Ma, D. Zhang, J. Zhan, Fe₃O₄@B-CD nanocomposite as heterogeneous Fenton-like catalyst for enhanced degradation of 4-chlorophenol (4-CP), *Appl. Catal. B* 188 (2016) 113–122.
- [36] M. Massa, R. Haggblad, A. Andersson, Cation vacant Fe_{3-x-y}V_{x-y}O₄ spinel-type catalysts for the oxidation of methanol to formaldehyde, *Top. Catal.* 54 (2011) 685–697.
- [37] K. Routray, W. Zhou, C.J. Kiely, I.E. Wachs, Catalysis science of methanol oxidation over iron vanadate catalysts: nature of the catalytic active sites, *ACS Catal.* 1 (2011) 54–66.
- [38] Y. Yu, P. Ju, D. Zhang, X. Han, X. Yin, L. Zheng, C. Sun, Peroxidase-like activity of FeVO₄ nanobelts and its analytical application for optical detection of hydrogen peroxide, *Sens. Actuators B* 233 (2016) 162–172.
- [39] Y.V. Kaneti, M. Liu, X. Zhang, Y. Bu, Y. Yuan, X. Jiang, A. Yu, Synthesis of platinum-decorated iron vanadate nanorods with excellent sensing performance toward n-butylamine, *Sens. Actuators B* 236 (2016) 173–183.
- [40] B. Ozturk, G.S.P. Soylu, Synthesis of surfactant-assisted FeVO₄ nanostructure: characterization and photocatalytic degradation of phenol, *J. Mol. Catal. A: Chem.* 398 (2015) 65–71.
- [41] Y. Zhao, K. Yao, Q. Cai, Z. Shi, M. Sheng, H. Lin, M. Shao, 1; Hydrothermal route to metastable phase FeVO₄ ultrathin nanosheets with exposed {010} facets: synthesis, photocatalysis and gas-sensing, *CrystEngCommun* 16 (2014) 270–276.
- [42] L. Huang, L.Y. Shi, X. Zhao, J. Xu, H.R. Li, J.P. Zhang, D.S. Zhang, Hydrothermal growth and characterization of length tunable porous iron vanadate one-dimensional nanostructures, *CrystEngComm* 16 (2014) 5128–5133.
- [43] X.C. Wang, K. Maeda, A. Thomas, K. Takanabe, G. Xin, J.M. Carlsson, K. Domen, M. Antonietti, A metal-free polymeric photocatalyst for hydrogen production from water under visible light, *Nat. Mater.* 8 (2009) 76–80.
- [44] Q.Y. Nong, M. Cui, H.J. Lin, L.H. Zhao, Y.M. He, Fabrication, characterization and photocatalytic activity of g-C₃N₄ coupled with FeVO₄ nanorods, *RSC Adv.* 5 (2015) 27933–27939.
- [45] A. Š. Vuk, B. Orel, G. Dražič, F. Decker, P. Colombari, UV-Visible and IR spectroelectrochemical studies of FeVO₄ sol-Gel films for electrochromic applications, *J. Sol-Gel Sci. Technol.* 23 (2002) 165–181.
- [46] S. Martha, A. Nashim, K.M. Parida, Facile synthesis of highly active g-C₃N₄ for efficient hydrogen production under visible light, *J. Mater. Chem. A* 1 (2013) 7816–7824.
- [47] D. Pradhan, K.T. Leung, Controlled growth of two-dimensional and one dimensional ZnO nanostructures on indium tin oxide coated glass by direct electrodeposition, *Langmuir* 24 (2008) 9707–9716.
- [48] X.C. Wang, S. Blechert, M. Antonietti, 1; Polymeric graphitic carbon nitride for heterogeneous photocatalysis, *ACS Catal.* 2 (2012) 1596–1606.
- [49] M. Jourshabani, A. Badie, Z. Sharatiatinia, N. Lashgari, G. Mohammadi Ziarani, Fe supported SBA-16 type cage-like mesoporous silica with enhanced catalytic activity for direct hydroxylation of benzene to phenol, *Ind. Eng. Chem. Res.* 55 (2016) 3900–3908.
- [50] J. Xu, Q. Jiang, T. Chen, F. Wu, Y.X. Li, Vanadia supported on mesoporous carbon nitride as a highly efficient catalyst for hydroxylation of benzene to phenol, *Catal. Sci. Technol.* 5 (2015) 1504–1513.
- [51] J. Xu, Q. Jiang, J.K. Shang, Y. Wang, Y.X. Li, A Schiff-base-type vanadyl complex grafted on mesoporous carbon nitride: a new efficient catalyst for hydroxylation of benzene to phenol, *RSC Adv.* 5 (2015) 92531–92538.
- [52] L.Y. Hu, C. Wang, L. Ye, Y.A. Wu, B. Yue, X.Y. Chen, H.Y. He, Direct hydroxylation of benzene to phenol using H_2O_2 as an oxidant over vanadium-containing mesoporous carbon catalysts, *Appl. Catal. A* 154 (2015) 440–447.
- [53] P. Zhang, Y. Gong, H. Li, Z. Chen, Y. Wang, Selective oxidation of benzene to phenol by FeCl₃/mpg-C₃N₄ hybrids, *RSC Adv.* 3 (2013) 5121–5126.

[54] L. Hu, C. Wang, B. Yue, X. Chen, H. He, Direct hydroxylation of benzene to phenol using H_2O_2 as an oxidant over vanadium-containing nitrogen doped mesoporous carbon catalysts, *RSC Adv.* 6 (2016) 87656–87664.

[55] A. Jönsson, E. Wehtje, P. Adlercreutz, B. Mattiasson, Thermodynamic and kinetic aspects on water vs organic solvent as reaction media in the enzyme-catalysed reduction of ketones, *Biochim. Biophys. Acta* 1999 (1430) 313–322.

[56] J.N. Park, J. Wang, K.Y. Choi, W.Y. Dong, S.I. Hong, Hydroxylation of phenol with H_2O_2 over Fe^{2+} and/or Co^{2+} ion-exchanged NaY catalyst in the fixed-bed flow reactor, *J. Mol. Catal. A: Chem.* 247 (2006) 73–79.

[57] N.A. Alekar, V. Indira, S.B. Halligudi, D. Srinivas, S. Gopinathan, C. Gopinathan, Kinetics and mechanism of selective hydroxylation of benzene catalysed by vanadium substituted heteropolytungstate, *J. Mol. Catal. A: Chem.* 164 (2000) 181–189.

[58] L.Y. Hu, B. Yue, C. Wang, X.Y. Chen, H.Y. He, Enhanced catalytic activity over vanadium-containing silylated SBA-15 catalysts for styrene epoxidation and benzene hydroxylation, *Appl. Catal. A* 477 (2014) 141–146.

[59] Y. Wang, H. Li, J. Yao, X. Wang, M. Antonietti, Synthesis of boron doped polymeric carbon nitride solids and their use as metal-free catalysts for aliphatic; 1; C-H bond oxidation, *Chem. Sci.* 2 (2011) 446–450.

[60] C. Yang, Y. Chen, S. Zhao, R. Zhu, Z. Liu, Preparation of CoNC catalysts via heating a mixture of cobaltporphyrin and casein for ethylbenzene oxidation, *RSC Adv.* 6 (2016) 75707–75714.

[61] B. Lu, N. Cai, J. Sun, X. Wang, X. Li, J. Zhao, Q. Cai, Solvent-free oxidation of toluene in an ionic liquid with H_2O_2 as oxidant, *Chem. Eng. J.* 225 (2013) 266–270.

[62] M.Q. Yang, Y. Zhang, N. Zhang, Z.R. Tang, Y.J. Xu, 1; Visible-light-driven oxidation of primary C-H bonds over CdS with dual co-catalysts graphene and TiO_2 , *Sci. Rep.* 3 (2013) 3314.

[63] H. Li, R. Liu, S. Lian, Y. Liu, H. Huang, Z. Kang, Near-infrared light controlled photocatalytic activity of carbon quantum dots for highly selective oxidation reaction, *Nanoscale* 5 (2013) 3289–3297.

[64] D. Lawless, N. Serpone, D. Meisel, Role of hydroxyl radicals and trapped holes in photocatalysis. A pulse radiolysis study, *J. Phys. Chem.* 95 (1991) 5166–5170.

[65] P. Wardman, Reduction potentials of one electron couples involving free radicals in aqueous solutions, *J. Phys. Chem. Ref. Data* 18 (1989) 1637–1755.